ELSEVIER

PII:S0266-8920(96)00010-0

Prob. Engng Mech. Vol. 12, No. 1, pp. 9–31, 1997

0266-8920/97 $17.00+0.00

Analysis and Simulation Tools For Wind Engineering

Kurtis R. Gurley, Michael A. Tognarelli & Ahsan Kareem

Department of Civil Engineering and Geological Sciences, University of Notre Dame, Notre Dame, IN 46556, USA

This paper examines state-of-the-art analysis and simulation tools for applications to wind engineering, introduces improvements recently developed by the authors, and directions for future work. While the scope of application extends to a variety of environmental loads (e.g. ocean waves and earthquake motions), particular reference is made to the analysis and simulation of non-Gaussian features as they appear in wind pressure fluctuations under separated flow regions and non-stationary characteristics of wind velocity fluctuations during a gust front, a thunderstorm or a hurricane. A particular measured non-Gaussian pressure trace is used as a focal point to connect the various related topics herein. Various methods of non-linear system modeling are first considered. Techniques are then presented for modeling the probability density function of non-Gaussian processes. These include maximizing the entropy functional subject to constraints derived from moment information, Hermite transformation models, and the use of the Kac–Siegert approach based on Volterra kernels. The implications of non-Gaussian local wind loads on the prediction of fatigue damage are examined, as well as new developments concerning gust factor representation of non-Gaussian wind loads. The simulation of non-Gaussian processes is addressed in terms of correlation-distortion methods and application of higher-order spectral analysis. Also included is a discussion of preferred phasing, and concepts for conditional simulation in a non-Gaussian context. The wavelet transform is used to decompose random processes into localized orthogonal basis functions, providing a convenient format for the modeling, analysis, and simulation of non-stationary processes. The work in these areas continues to improve our understanding and modeling of complex phenomena in wind related problems. The presentation here is for introductory purposes and many topics require additional research. It is hoped that introduction of these powerful tools will aid in improving the general understanding of wind effects on structures and will lead to subsequent application in design practice.

BACKGROUND

Over the last few decades, our understanding of wind–structure interactions and resulting load effects has significantly improved, yet a need remains for further examination of a host of issues. Many of the studies encompassing analysis and modeling of wind effects on structures have tacitly assumed that the involved random processes are Gaussian. This assumption has been invoked primarily for the convenience in analysis, since information concerning statistics of Gaussian processes is abundant. This assumption is quite valid for loads that involve integral effects of the random pressure field over large areas. Nonetheless, regions of structures under separated flows experience strong non-Gaussian effects in the pressure distribution characterized by high skewness and kurtosis. The non-Gaussian effects in pressure result in non-Gaussian local loads, and give way to increased expected damage in glass panels and higher fatigue effects on other components of cladding.

The probabilistic analysis of pressure fields has been of interest to those involved in wind tunnel studies. Peterka and Cermak[1] and Kareem[2] demonstrated that in pressure regions where the mean pressure was below -0.25, the pressure probability density functions (pdf) are skewed such that the probabilities for large negative fluctuations are much higher than those for Gaussian processes. Similar observations have also been reported by others. It was also noted that due to non-linear relationships between wind and pressure fluctuations the pdf of pressure under high turbulence may be non-Gaussian. Low-rise structures immersed in the highly turbulent lower part of the boundary layer, whose structure is further invigorated by the presence of roughness elements in the surroundings, may experience non-Gaussian pressure fluctuations even on their windward faces. These non-Gaussian effects may be amplified further as the approaching wind fluctuations may depart from a Gaussian process. Similar effects are observed in wave effects on structures.[3] Holmes[4] and Kuwai[5] utilizing quasi-steady and strip theories evaluated the derived pdf of pressure. The resulting distribution showed good agreement with measured data on the surfaces with attached flows. However, as expected, the derived pdf of pressures in the separated regions is not predicted by the quasi-steady theory as the wind–structure interactions at several scales of turbulence may introduce additional components. This observation is again corroborated by Letchford *et al.*[6] utilizing full-scale data. In an attempt to identify admittance functions for wind pressures, Thomas *et al.*[7] have noted that the quasi-steady theory fails to model spectral descriptions of pressures under separated regions despite the inclusion of the square of the fluctuating velocity term. Similar comments are offered by Tieleman and Hajj[8] based on their analysis of full-scale data. In summary, the quasi-steady theory offers reliable estimates of load effects when the dominant mode of loading is attributed to buffeting, e.g. surface pressures responding to large-scale low frequency turbulence. However, the pressures resulting from wind–structure interaction effects cannot be predicted from the quasi-steady theory. A departure from the quasi-steady theory is reflected in the non-Gaussian field.

In light of the established inability of quasi-steady theory to predict the dynamics and probabilistic structure of pressure fluctuations in the separated regions, some thoughts on the modeling of non-Gaussian processes are presented. This approach holds promise for providing answers and perhaps models for situations in which the quasi-steady theory has failed to do so because pressure fluctuations are a result of a non-linear dynamic interaction.

The analysis of a non-stationary processes such as transient wind gusts in short, measured wind records have been limited due to shortcomings in the Fourier analysis. Here, we apply a set of basis functions local in both time and frequency to decompose the signal into octave-banded constitutive parts. The wavelet transform is useful in the location of energy transfer in time, and in the simulation of non-stationary processes.

MODELING OF NON-GAUSSIAN PROCESSES

In the study of physical systems, the relationship between the input and the system output is often sought to model the system response. For linear systems, e.g. in the formulation of gust loading factors such a relationship is used for the prediction of extreme response.[9] In many instances in wind engineering, however, the input and output are not related by a linear transfer function due to non-linear characteristics, e.g. the turbulent fluctuations in a hurricane, negative pressure fluctuations on building envelopes and associated fatigue of cladding and, in particular, its fastening system. Many approaches are available for modeling non-linearly related processes. Here we present a brief look at Volterra series systems, as well as several other alternatives.

Volterra systems

In the Volterra series formulation, the input–output relationship may be expressed in terms of a hierarchy of linear, quadratic and higher-order transfer functions or impulse response functions (e.g. Refs 10–13). These transfer functions can be determined from experimental data or from theoretical considerations. For example, a non-linear system modeled by Volterra's stochastic series expansion is described by

$$y(t) = \int h_1(\tau)x(t-\tau)\mathrm{d}\tau + \int\int h_2(\tau_1,\tau_2)x(t-\tau_1) \times x(t-\tau_2)\mathrm{d}\tau_1\mathrm{d}\tau_2 + \ldots \quad (1)$$

where $h_1(\tau)$ and $h_2(\tau_1,\tau_2)$ are the first and second-order impulse response functions.

The Fourier transform of the Volterra series expansion up to second order (retaining two terms on the right hand side) in eqn (1) gives the response in the frequency domain as

$$Y(f_i) = H_1(f_i)X(f_i) + \sum_{f_1+f_2=f_i} H_2(f_1,f_2)X(f_1)X(f_2) \quad (2)$$

For linear systems, the first term on the right hand side of eqn (2) is all that is needed to describe the relationship between input and output. This linear model assumes that the Fourier components at different frequencies are uncoupled. In the first (linear) term on the right hand side of eqn (2) the response $Y(f_i)$ at frequency f_i is dependent only on input and the transfer function at frequency f_i.

In the case where the system is non-linear, the Fourier components are coupled, and additional terms are needed to capture this interaction. The second term on the right hand side of eqn (2) couples the response $Y(f_i)$ at frequency f_i with pairs of input components at frequencies whose sum or difference is f_i through the quadratic transfer function (QTF) $H_2(f_1,f_2)$. Equation (2) describes a system whose non-linear component is non-symmetric with respect to the probability density function (e.g. an even powered polynomial non-linearity). A third-order system captures the behavior of systems with both symmetric and non-symmetric non-linearities (e.g. polynomial non-linearities with odd and even powers).

In the case when input $x(n)$ and output $y(n)$ of a system is available, the information can be used to estimate the Volterra kernels in eqn (2) directly. The linear transfer function is given by

$$H_1(f_i) = \frac{\langle X^*(f_i)Y(f_i)\rangle}{\langle |X(f_i)|^2\rangle} \tag{3}$$

where $\langle\ \rangle$ is the expected value operator. Here, the numerator is the cross-power spectrum of the input $x(n)$ and output $y(n)$ in terms of their Fourier transforms $Y(f)$ and $X(f)$, and the denominator is the auto-power spectrum of the input.

Just as $H_1(f_i)$ is derived from the cross-power spectrum, the QTF is derived from a higher-order cross-spectrum. The higher-order cross-spectrum between the input $x(n)$ and the output $y(n)$ needed to estimate the QTF is called the cross-bispectrum, denoted $B_{xxy}(f_1,f_2)$. Analogous to the cross-power spectrum in the numerator of eqn (3), the cross-bispectrum can be expressed in terms of the expected value of input and output Fourier components as

$$B_{xxy}(f_1,f_2) = \langle X^*(f_1)X^*(f_2)Y(f_1+f_2)\rangle \tag{4}$$

The QTF is given by

$$H_2(f_1,f_2) = \frac{1}{2}\frac{B_{xxy}(f_1,f_2)}{\langle |X(f_1)X(f_2)|^2\rangle} \tag{5}$$

If no phase coupling exists between $Y(f_1+f_2)$ and $X(f_1)$ and $X(f_2)$, then their phases will be random and independent, thus the net expected value of the cross-bispectrum will be zero. The formulation for the QTF given in eqn (5) is valid for a Gaussian input process $X(f)$. The linear and quadratic transfer functions can also be estimated for a general random input, i.e. without assuming particular statistics of the input (e.g. Ref. 14).

Equation (2) addresses a second-order Volterra system, which assumes the non-linearity is asymmetric. More generally, higher-order spectral analysis may be applied to non-linear system identification via the higher-order transfer function, which may then be used with a Volterra series similar to eqn (2) with additional higher-order terms to model the non-linear system.

The analogies between the power spectrum and higher-order spectra may be extended to glean some insight into their physical meaning. The significance of the power spectrum $S_{xx}(f_1)$ is well understood to be the decomposition of the signal variance $\langle x^2(t)\rangle$ as a function of frequency. Similarly, the bispectrum $B_{xxx}(f_1,f_2)$ may be viewed as the decomposition of skewness ($\langle x^3(t)\rangle$ as a function of two frequencies, and the trispectrum $T_{xxxx}(f_1,f_2,f_3)$ as the decomposition of kurtosis $\langle x^4(t)\rangle$ as a function of three frequencies. The volumes under the bispectrum and trispectrum yield the third and fourth central moments, respectively. When viewed in this light, it is apparent that the existence of higher-order spectra indicates a deviation from Gaussian.

An estimated bispectrum for an experimentally measured wind pressure record is shown in Fig. 1. This non-zero bispectrum indicates a deviation from Gaussian due to interaction between low frequency

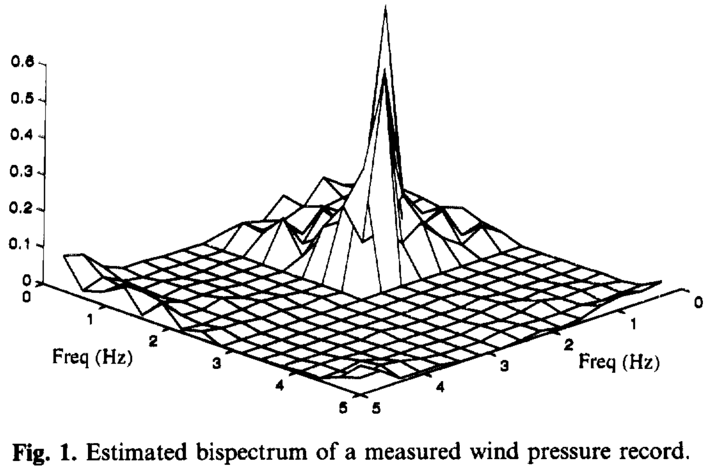

Fig. 1. Estimated bispectrum of a measured wind pressure record.

components. For a quadratic non-linear process that is a square of a narrow-banded linear process, the bispectrum contains peaks where components of the linear process interact at their sum and difference frequencies, imparting energy at those frequencies to the resulting non-linear process. In this case, the bispectrum does not consist only of sharp peaks, indicating that the pressure record is not the result of the square of a narrow-banded process, but more likely the output of an at least partially quadratic system with a wide-banded input. The input process in this case is in fact a wide-banded wind velocity process. Were it the case that pressure was the result of a cubic non-linearity acting on the wind velocity, the bispectrum would not exist, and the trispectrum would reveal the symmetrically non-linear relation of the pressure to velocity.

Alternatives to Volterra systems

Several researchers have addressed the modeling of non-linear systems by means other than a Volterra series expansion and application of higher-order spectra. For example, Bendat[15] replaced the higher-order frequency domain contribution in eqn (5) by a zero-memory squared term in series with a linear term. Non-linear pressure on a building from Gaussian wind velocity input is modeled in this fashion to improve upon the modified quasi-steady theory by using a multiple admittance function.[7] Here, the pressure autospectrum is expressed in terms of the spectra of the horizontal and vertical fluctuating wind components, the spectra of these components squared, and transfer functions in terms of the cross-spectra of the inputs with measured pressure output. Bendat's model replaces the second-order Volterra kernel by a linear kernel based on the assumption that the QTF is constant along lines normal to the diagonal as in

$$H_2(f_1,f_2) = A(f_1+f_2) \tag{6}$$

This is equivalent to all frequency pairs for a particular sum or difference frequency containing the same level of phase coupling. This assumption conveniently reduces, for example, a single input/single output second-order Volterra model to a two input/single output linear model. The efficiency of the analysis is advantageous, and retains limited memory. The error associated with this representation is lumped into a noise or residual spectrum which is minimized with respect to the transfer functions describing the linear systems in parallel. The non-linearity is represented, but the assumption of its form may be restrictive for some systems. The model may be modified to facilitate the input of non-Gaussian wind velocity.[15]

Neural networks

Another recently developed approach to non-linear system modeling is the application of neural networks. A multi-layered set of processing elements receives input information and uses the desired final output information to adjust a weighting factor between each of the elements. Figure 2 shows such a network with three weighting layers $W_{ij}(m)$, $m = 1,\ldots,3$, where $i = 1\ldots N_m$, $j = 1,\ldots,N_{m-1}$, and N_m and N_{m-1} are the number of elements in the mth and the $m-1$th layers, respectively. The network in Fig. 2 has two hidden element layers $a_i(1)$ and $a_i(2)$ between the input and output layers $a_i(0)$ and $a_i(3)$. In this example, the input layer consists of the input occurring at the same time as the current output from $a_1(3)$, and two delayed inputs. $W_{ij}(m)$ then represents the weighting of the output from the element $a_j(m-1)$ before its input to element $a_i(m)$. The output of each element $b_i(m)$ is a non-linear function of the weighted linear sum of the output from each of the elements in the previous layer as in[16]

$$b_i(m) = \sum_{j=1}^{N_{m-1}} W_{ij}(m)a_j(m-1) + \theta_i(m)$$
$$a_i(m) = f(b_i(m)) \quad 1 \le i \le N_m \quad 1 \le m \le 3 \tag{7}$$

where $\theta_i(m)$ is a threshold value fixed for each $a_i(m)$. Various non-linear functions may be applied at the elements. One commonly applied function is the sigmoid function

$$f(b_i) = \frac{1}{1+e^{-b_i/\sigma}} \tag{8}$$

where σ is a parameter to control the shape of $f(b_i)$.

The element weights in the neural network are adjusted iteratively to minimize the error between the resulting and desired final output. This is the training phase, in which the optimum model parameters $W_{ij}(m)$, $m = 1,\ldots,M$ are identified, where M is the number of network layers, and $M = 3$ for the example in Fig. 2.[16]

An example application is shown in Figs 3 and 4. In Fig. 3, the input is a simulated Gaussian wind velocity $(U + u(t))$ sampled at 100 Hz for 10 s, and the output is the resulting force on a unit area using $F = \rho C_d A(U + u(t))^2/2$. The neural network has two

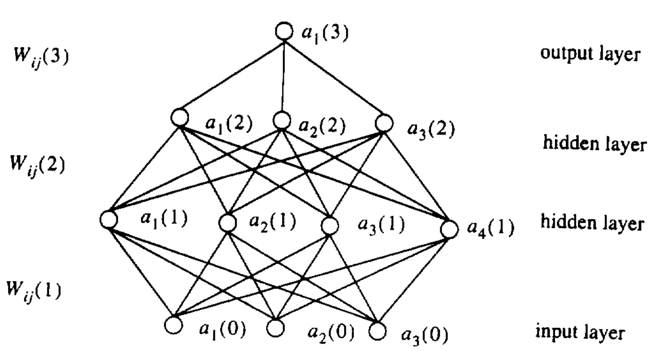

Fig. 2. Multilayer neural network with three weighting layers and two hidden layers (adapted from Kung[16]).

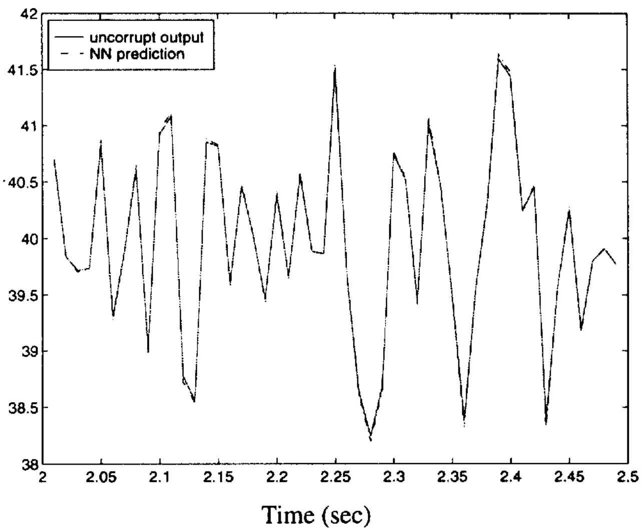

Fig. 3. Noiseless force output and neural network model prediction.

hidden layers of 25 and 30 elements, respectively, with a two delay input. The network is given the first second of input/output data to train itself with, and the figures present the model prediction of later unknown output given wind velocity input. In Fig. 4, a Gaussian white noise is added to the force output to represent measurement noise. The neural network does not exactly model the input/output with noise, but closely approximates the uncorrupted output. These results will vary as the neural network architecture is altered, such as varying the number of elements in the layers, changing the number of delays, etc.[17,18]

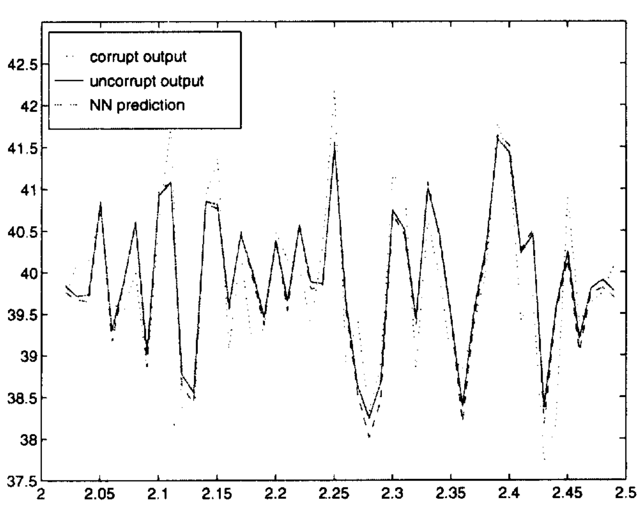

Fig. 4. Noise corrupted force output, neural network model prediction of corrupt output, and uncorrupt force output.

MODELING OF PROBABILITY DENSITY FUNCTION

The modeling of the probabilistic structure of non-Gaussian pressure fluctuations is essential for a wide range of applications in wind engineering, e.g. accurate determination of design wind pressure for glass panels. Large skewness results in probabilities for negative pressure fluctuations much higher than those for Gaussian processes. Series distribution methods, including Gram–Charlier, Edgeworth, and Longuet–Higgins, based on Hermite polynomials, have been commonly used (e.g. Ref. 19), but tend to exhibit oscillating and negative tail behavior. For extreme response, alternative means are considered.

The non-Gaussian distribution derived based on the non-linear relationship between wind and pressure fluctuations with the assumption of Gaussian velocity is valid mostly for windward and leeward faces. This has been shown to fail in separated regions over surfaces parallel to wind flow, where quasi-steady theory breaks down. The lognormal distribution has been used in the literature to model pressure data as the tail of the distribution is higher than for the normal distribution. This often provides values close to the observations, but still fails to predict the occurrence of values far from the mean. Calderone *et al.*[20] recently noted that the lognormal distribution does not fit the pressure data perfectly.

In view of the preceding shortcomings, three alternative approaches to modeling the pdf of non-Gaussian pressure fluctuations in separated regions are considered here. The maximum entropy method (MEM), Hermite transformation-based models and Kac–Siegert expansion-based models are applied to the pressure records through their statistical moments or quadratic transfer function to determine the parameters of the respective estimation models. Applications of these methods are illustrated by way of two examples.

Maximum entropy method

An approach to approximate the pdf of non-linear systems is the maximum entropy method (MEM), in which the Shannon entropy functional is maximized subject to constraints in the form of moment information. In the limiting case of infinite moment information, a unique pdf is defined. In reality, we will always have a finite amount of moment information for which an infinite number of probability density functions are admissible. The pdf which maximizes the entropy functional is the least biased estimate for the given moment information. The Lagrange multiplier method is applied to solve this variational problem, and provides the joint pdf of higher-order systems directly. A brief outline of MEM is presented here. Complete details can be found in Sobczyk and Trebicki[21], Kareem and Zhao[13] and Kapur.[22]

The available information for a process $y(t)$ can be expressed as the process joint moments

$$E[y_1^{r_1}y_2^{r_2}\dots y_n^{r_n}] = \int\dots\int y_1^{r_1}y_2^{r_2}\dots y_n^{r_n}p(y)\,\mathrm{d}y = m_{r_1\dots r_n} \tag{9}$$

where n is the order of the system. $r_i = 0.1, 2, \dots, M$, where M is the maximum order or correlation moment, $p(y)$ is the joint pdf, and $m_{r_1\dots r_n}$ is the value of the joint moment. The integral is multifold to n. One possible pdf of the process $y(t)$ is that which maximizes the entropy functional

$$H = -\int p(y)\ln p(y)\,\mathrm{d}y \tag{10}$$

subject to constraints from the moment information.

After application of the Lagrange multiplier method, the resulting description of $p(y)$ for an n-dimensional case is

$$p(y) = \exp(-\lambda_0 - 1)\exp\left(-\sum_{r_1+\dots+r_n}^{M} \lambda_{r_1\dots r_n} y_1^{r_1}\dots y_n^{r_n}\right) \tag{11}$$

Substitution of eqn (11) into the moment constraints and an additional normalization constraint $\int p(y)\mathrm{d}y = 1$ gives the following system of equations:

$$\int y_1^{r_1}\dots y_n^{r_n}\exp\left(-\sum_{r_1+\dots+r_n}^{M} \lambda_{r_1\dots r_n} y_1^{r_1}\dots y_n^{r_n}\right)\mathrm{d}y = m_{r_1\dots r_n} \tag{12}$$

$$\int \exp\left(-\sum_{r_1+\dots+r_n}^{M} \lambda_{r_1\dots r_n} y_1^{r_1}\dots y_n^{r_n}\right)\mathrm{d}y = \exp(\lambda_0 + 1) \tag{13}$$

This system of non-linear integral equations is solved numerically and the results yield the least biased estimate of the system joint pdf under the given moment constraints using eqn (11).[13,21] The moment information which constrains the maximum entropy functional may be in the form of moment equations rather than moment values as presented above. Details are omitted here, interested readers may refer to Sobczyk and Trebicki.[21]

Moment-based Hermite transformation model

This approach is based on a functional transformation of a standardized non-Gaussian process, $x(t)$, to a standard Gaussian process, $u(t)$, (e.g. Ref. 23)

$$x(t) = (X(t) - \bar{X})/\sigma_X = g[u(t)] \tag{14}$$

Several choices of $g(u)$ are possible to preserve only the first four moments. A cubic model of $g(u)$ offers a convenient and fairly accurate representation.[24] Accordingly, the pdf of $x(t)$ is given by[23,24]

$$p_x(x) = \frac{1}{\sqrt{2\pi}}\exp\left[-\frac{u^2(x)}{2}\right]\frac{\mathrm{d}u(x)}{\mathrm{d}x} \tag{15}$$

$$u(x) = \left[\sqrt{\xi^2(x) + c} + \xi(x)\right]^{1/3} - \left[\sqrt{\xi^2(x) + c} - \xi(x)\right]^{1/3} - a \tag{16}$$

where $\xi(x) = 1.5b(a + \frac{x}{\alpha}) - a^3$

$$a = \frac{\hat{h}_3}{3\hat{h}_4}, \quad b = \frac{1}{3\hat{h}_4}, \quad c = (b - 1 - a^2)^3$$

$$\hat{h}_3 = \frac{\Gamma_3}{4 + 2\sqrt{1 + 1.5\gamma_4}}, \quad \hat{h}_4 \frac{\sqrt{1 + 1.5\gamma_4} - 1}{18}$$

$$\alpha = \frac{1}{\sqrt{1 + 2\hat{h}_3^2 + 6\hat{h}_4^2}}$$

and γ_3 and γ_4 are the skewness and kurtosis of the fluctuating process, which reduce to zero for Gaussian. An improvement to this model is suggested here by using the expressions for $\hat{h}_3$ and $\hat{h}_4$ given previously (which are approximations) as initial conditions for solving the following pair of non-linear algebraic equations:

$$\gamma_3 = \alpha^3(8\hat{h}_3^3 + 108\hat{h}_3\hat{h}_4^2 + 36\hat{h}_3\hat{h}_4 + 6\hat{h}_3) \tag{17}$$

$$\gamma_4 + 3 = \alpha^4(60\hat{h}_3^4 + 3348\hat{h}_4^4 + 2232\hat{h}_3^2\hat{h}_4^2 + 60\hat{h}_3^2 + 252\hat{h}_4^2 + 1296\hat{h}_4^3 + 576\hat{h}_3^2\hat{h}_4 + 24\hat{h}_4 + 3) \tag{18}$$

These equations have been derived for use in this study by setting the third- and fourth-order central moments of $g[u(t)]$ equal to the known central moments of $x(t)$. This yields new coefficient values which exactly match the statistics up to the fourth order of the modeled non-Gaussian process. This is referred to herein as the modified Hermite method.

The transformation above is for the case when $x(t)$ is a softening process, for example, the response of a linear system subjected to non-linear viscous drag force. Winterstein[24] also outlines a transformation for the case in which $x(t)$ is a hardening process. This development is not repeated here, but such a situation could arise, for example, if the structural system is characterized by a non-linear stiffness.

Kac–Siegert approach

Once a system has been modeled in terms of a Volterra series (eqn (1)), different approaches are available to estimate the pdf of the process. One such approach is that of Kac and Siegert.[25] In this approach, the system output is expressed in terms of the sum of standardized normal random variates X_j and their squares as described below (e.g. Refs 13, 26, 27)

$$y(t) = \sum_{j=1}^{2N}(B_jX_j + \lambda_jX_j^2) \tag{19}$$

The parameter B_j is related to the eigenvectors ψ_j, and λ_j are the eigenvalues of the Fredholm integral equation of the second kind given by

$$\int K(\omega_1,\omega_2)\psi_j(\omega_2)\mathrm{d}\omega_2 = \lambda_j\psi_j(\omega_1)$$

$$K(\omega_1,\omega_2) = H(\omega_1,\omega_2)\sqrt{S(\omega_1)S(\omega_2)} \tag{20}$$

where $H(\omega_1,\omega_2)$ is the QTF discussed earlier, and the frequency domain counterpart of $h_2(\tau,\tau_2)$, and $S(\omega)$ is a two-sided spectrum of the underlying linear process.

The characteristic equation of x is now expressed as

$$M(\theta) = \prod_{j=1}^{2N} M_j(\theta)$$

$$\text{where } M_j(\theta) = (1 - 2i\lambda_j)^{-1/2}\exp\left[-\frac{B_j^2\theta^2}{2(1-2i\lambda_j\theta)}\right] \tag{21}$$

The pdf of the process x is the Fourier transform of the characteristic function

$$p(x) = \frac{1}{2\pi}\int_{-\infty}^{\infty} \mathrm{e}^{-i\theta x}M(\theta)\mathrm{d}\theta \tag{22}$$

In general, eqn (22) cannot be solved in closed form, and must be numerically estimated. This representation of a non-Gaussian pdf is most appropriate for non-Gaussian systems resulting from a quadratic transformation. Any other transformation must be recast in a quadratic form to obtain the best results.

The nth cumulant k_n of a random process y is defined in terms of the characteristic function and after appropriate substitutions is given by

$$k_n = \sum_{j=1}^{2N} 1/2(2\lambda_j)^n\left\{(n-1)! + \left(\frac{B_j}{2\lambda_j}\right)^2 n!\delta_{n1}\right\} \tag{23}$$

where δ_{n1} is zero for $n = 1$, and unity otherwise. These cumulants may be used as coefficients in a series of expansion of the pdf, or as constraints in the maximum entropy method.

Examples

An application of the MEM, Hermite moment, Kac–Siegert, and Gram–Charlier polynomial series methods of pdf estimation are shown along with a Gaussian model in Fig. 5, where the process is the non-linear response of an offshore platform to random wind loads.[13] The inset is a view of the tail of the pdf on a logarithmic scale, in which the higher probability of extreme response in a softening non-linear system can be observed. In applying the Kac–Siegert technique, 128 discrete frequencies are used resulting in 256 and 128 values of λ and B, respectively, to form the characteristic function in eqn (21). Discretization finer than this does not noticeably improve results in this example. Equation (23) is used to produce the cumulant values used in the MEM, Hermite moment, and Gram–Charlier Hermite polynomial methods. In this example, the skewness and kurtosis are 0.3829 and 0.2066, respectively. Deviation from Gaussian is not large in this case. All methods give approximately the same prediction

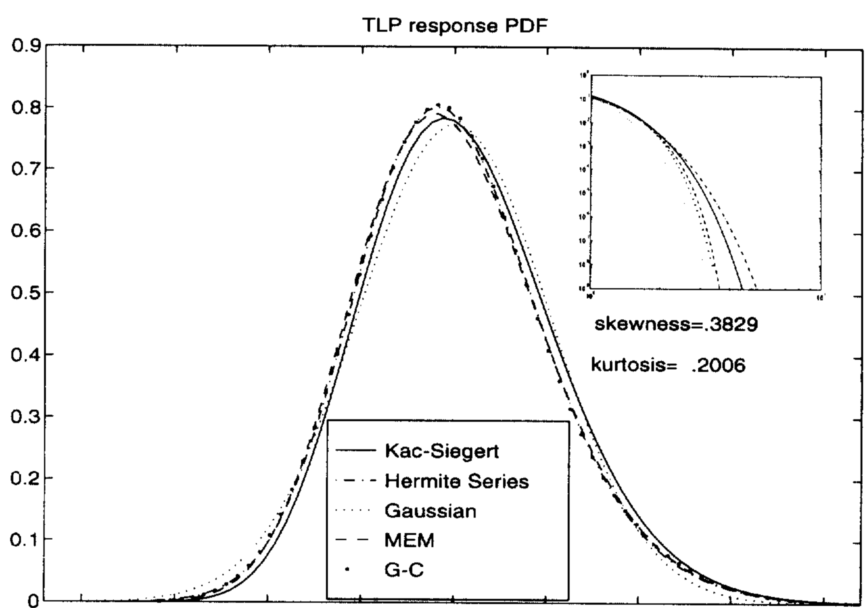

Fig. 5. Kac–Siegert, Hermite moment, MEM, Gram–Charlier and Gaussian pdf estimates of nonlinear response.

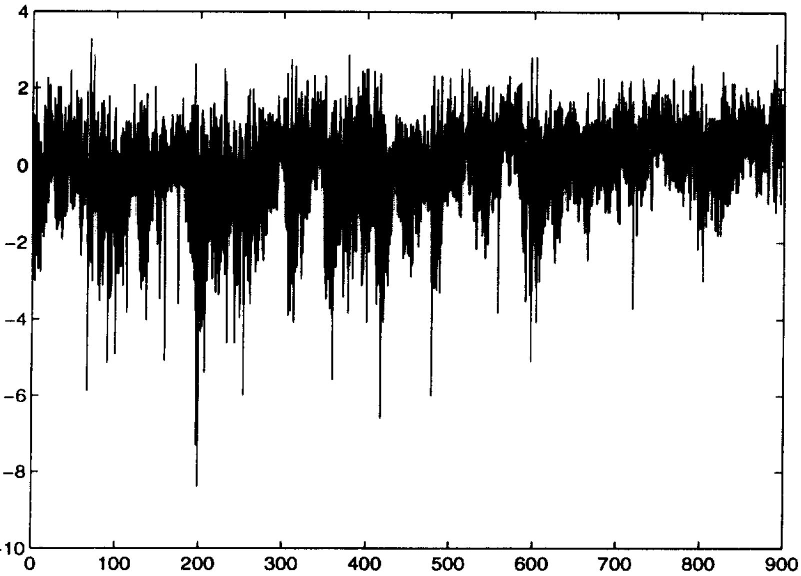

Fig. 6. Measured non-Gaussian pressure trace.

in the mean region, while the Kac–Siegert and Hermite moment tend to provide more conservative estimates in the tail region (inset).

The second example concerns the measured pressure fluctuations on a full-scale low-rise building.[7] The pressure data, histogram, a fitted Hermite moment model, and a lognormal fit are given in Figs 6 and 7. The skewness and kurtosis are reported in Table 1 along with the parameters used in the Hermite transformation of eqn (16). In this case, the deviation from Gaussian is large, and the modified Hermite moment model fits the histogram well. The negative tail region is shown in the inset, where the close fit of the extremes of the data by the Hermite moment model contrasts that of the Gaussian tail. A lognormal fit utilized by Calderone *et al.*[20] is also shown on this figure and while it predicts the tail region more accurately than the Gaussian distribution, it falls well short of equalling the effectiveness of the moment-based Hermite transformation in quantifying the extremes of the distribution. A Kolmogorov–Smirnov goodness-of-fit test also confirms the superior fit of the Hermite moment model.

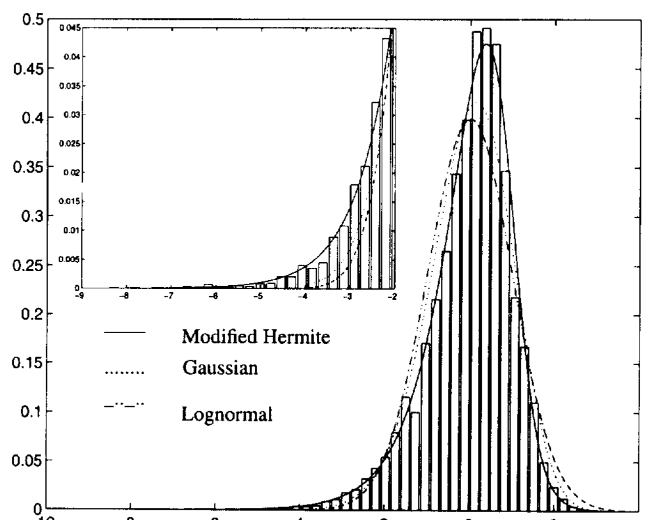

Fig. 7. Histogram, Gaussian fit, lognormal fit, and modified hermite moment based pdf estimate of data shown in Fig. 6.

APPLICATIONS OF PDF MODELS

Fatigue/glass damage

Typically, the fatigue damage caused by wind-induced fluctuations due to non-Gaussian gusts or pressures under separated flow regions is assessed based on the assumption that the underlying process is Gaussian. These results may considerably underestimate fatigue damage for some regions on a building envelope. Based on the models involving Volterra series, or information on the skewness and kurtosis of a process, a systematic correction factor can be added to the Gaussian fatigue damage estimate that reflects the effects of non-Gaussianity. A simple measure of the influence of non-Gaussian effects on fatigue damage accumulation is the ratio of fatigue damage under non-Gaussian loading to that under Gaussian loading

$$\lambda = \frac{E[D_n g]}{E[D_g]} \tag{24}$$

Table 1. Coefficients used in eqn (16) for Hermite moment fit of pressure data

Skewness γ_3	Kurtosis γ_4	a	b	c	$\hat{h}_3$	$\hat{h}_4$	α
−0.9869	2.3278	−1.358	9.660	317.4	−0.1403	0.0345	0.9775

This ratio, based on Hermite moment transformation models for the non-Gaussian narrow-banded processes, is given by Winterstein[24] as

$$\lambda = \left(\frac{\sqrt{\pi}k}{2V_s!}\right)^m \left(\frac{(mV_s)!}{(m/2)!}\right) \quad V_s = \frac{4}{\pi}(1 + h_4 + \hat{h}_4) - 1 \tag{25}$$

where $h_4 = \gamma_4/24$, $k = (1 + 2\hat{h}_3^2 + 6\hat{h}_4^2)^{-1/2}$, and $\hat{h}_3$ and $\hat{h}_4$ have been defined in eqn (16). Utilizing the non-Gaussian pressure fluctuation data in Fig. 6, λ is equal to 1.6. This could potentially enhance fatigue of cladding components by 60 percent. The assumption of normality may lead to unconservative fatigue life prediction when the actual response is non-Gaussian with a kurtosis value greater than zero. However, conservative estimates are expected for non-Gaussian cases with a kurtosis value less than zero.

The importance of non-Gaussian local pressures on cladding glass has been addressed by, among others, Holmes,[28] Reed,[29] and Calderone and Melbourne.[30] Holmes[28] and Reed[29] utilized a non-Gaussian distribution of pressure fluctuations based on the relationship between Gaussian wind velocity and non-Gaussian pressure variations. This relationship is based on quasi-steady theory which has its limits but works well for stagnation face pressure. Numerical simulations involving wind tunnel data have revealed that non-Gaussian fluctuations result in greater glass damage. The cumulative damage criterion is used to determine the effect of fluctuating pressure through an equivalent constant pressure. Beside the non-linear relationship between the pressure and resulting stress in glass, the glass size, and its geometry, the non-Gaussian features of pressure fluctuations play an important role in determining the cumulative damage. The equivalent constant pressure is given by[28]

$$p_{\rm E} = \left(\frac{1}{T_{\rm E}}\sum_{i=1}^{l} p_i^{sn} t_i\right)^{\frac{1}{sn}} = \left[T_{\rm s}\left(\frac{1}{T_{\rm E}}\int_{-\infty}^{\infty} p^{sn} f_{\rm p}(p)\,{\rm d}p\right)\right]^{\frac{1}{sn}} \tag{26}$$

where $T_{\rm E}$ is the duration of the equivalent pressure (60 s in the U.S.), p_i is the pressure at a particular instant, l is the total number of instants being accumulated, t_i is the time duration of pressure p_i, s is the slope of the straight line on a log–log scale of the plot between pressure and surface tensile strength of glass, and n is dependent on the type of glass.[30] In the second expression for $p_{\rm E}$, $T_{\rm s}$ is the length of the sample considered and $f_{\rm p}(p)$ is the pdf of the pressure process. Using a histogram of a sample of data ($T_{\rm s} = 900$ s) to represent the pdf of the data, the ratio of $P_{\rm E}$ for the non-Gaussian model to Gaussian is equal to 1.84. Using the Hermite moment model, this ratio is 1.76 and using a lognormal model[30] the ratio is 1.18. For comparison's sake, the limits of the integration have been taken to be the end points of the range for which pressure data is available in the realization of data considered. This illustrates the significance of non-Gaussian effects in the evaluation of $p_{\rm E}$ and more importantly the effectiveness of the moment-based Hermite transformation in capturing this significance.

Gust factors

The use of gust factors to account for the dynamics of wind fluctuations is accepted worldwide. The concept, based on the original formulation by Davenport,[9] relies on the assumption of a Gaussian process. For dynamic pressures resulting from the square of wind velocity the Gaussian assumption may break down. Soize[31] and Kareem and Zhao[13] have extended Davenport's Gaussian model to include non-Gaussian effects, which are more pronounced for relatively stiffer structures. The non-Gaussian contribution also increases for high levels of turbulence. The gust factor, G, relates the mean of the extremes of a process to the mean of the parent process as follows:

$$\bar{X}_{\rm ex} = \bar{X} + g\sigma = \bar{X}\left(1 + \frac{g\sigma}{\bar{X}}\right) = G\bar{X} \tag{27}$$

where g is the peak factor. When $\bar{X} = 0$, we simply have $\bar{X}_{\rm ex} = g\sigma$ and we need merely to compute the peak factor. The peak factor used in the non-Gaussian gust factor formulation[13] employs the moment-based Hermite transformation which has been shown to be more accurate in representing the tail regions of the pdf of a non-Gaussian process than the Edgeworth series employed by Soize.[31] Treating the standardized non-Gaussian random variable as a non-linear function of a Gaussian random variable as in eqn (14), the probability density function of the process X may be readily derived (e.g. Ref. 32).

According to Cartwright and Longuet-Higgins,[33] the distribution of all maxima (positive and negative) of the standardized Gaussian process are given as

$$\begin{aligned} p_{U_{\max}}(u) = \frac{1}{\sqrt{2\pi}}\Bigg[&\varepsilon \exp\left(-\frac{u^2}{2\varepsilon^2}\right) \\ &+ \sqrt{1-\varepsilon^2}\,u \exp\left(-\frac{u^2}{2}\right)^u \\ &\times \int_{-\infty}^{u\frac{\sqrt{1-\varepsilon^2}}{\varepsilon}} \exp\left(-\frac{\xi^2}{2}\right){\rm d}\xi\Bigg] \end{aligned} \tag{28}$$

where $\varepsilon = \sqrt{1 - m_2^2/(m_0 m_4)}$ is a descriptor of the bandwidth of the parent Gaussian process and the m_i can be described in terms of moments of the one-sided spectral density of the process, $m_i = \int_0^\infty n^i S(n){\rm d}n$, where n is frequency in Hertz. For a narrow-banded process, $\varepsilon = 0$, and eqn (28) yields the Rayleigh distribution.

The cumulative distribution of the extremes of the parent Gaussian process is (e.g. Refs 9,34)

$$P_{U_{ex}}(u) = \exp[-N(1 - P_{U_{max}}(u))] \quad (29)$$

where $N = \sqrt{m_4/m_2}T$ is the expected number of maxima during an interval of length, T (e.g. Ref. 35), and from eqn (28) assuming that u is large, we may approximate[33]

$$1 - P_{U_{max}}(u) \approx \sqrt{1-\varepsilon^2}\exp\left(-\frac{u^2}{2}\right) + O\left(\frac{1}{u^3}\exp\left(-\frac{u^2}{2\varepsilon^2}\right)\right) \approx \frac{m_2}{\sqrt{m_o m_4}}\exp\left(\frac{-u^2}{2}\right) \quad (30)$$

which leaves

$$P_{U_{ex}}(u) = \exp\left[-\sqrt{m_2/m_0}T\exp\left(-\frac{u^2}{2}\right)\right] \quad (31)$$

So, we have for the extremes of X

$$P_{X_{ex}}(x) = \exp\left[-\sqrt{m_2/m_0}T\exp\left(-\frac{u^2(x)}{2}\right)\right] \quad (32)$$

The peak factor, g_{ng}, relates the mean of the positive extreme values of X to its standard deviation. To compute it, we must first determine $\mathrm{d}P_{X_{ex}}(x)$. Making the assumption in eqn (30), we have for the case when X is zero mean

$$\mathrm{d}P_{X\mathrm{ex}}(x) = \exp(-\psi)\mathrm{d}\psi, \quad \psi = \nu_0 T\exp[-u^2(x)/2]$$
$$\text{and } \nu_0 = \sqrt{m_2/m_0} \quad (33)$$

This gives

$$\bar{X}_{ex} = \int_0^\infty x(\psi)\exp(-\psi)\mathrm{d}\psi = g_{ng}\sigma_x \quad (34)$$

In order to evaluate eqn (34), we must develop the form of $x(\psi)$. This is accomplished by first solving for $u(x)$, according to

$$u(x) = \sqrt{2\ln\nu_0 T - 2\ln\psi} \quad (35)$$

Since the time, T, is usually very large, an asymptotic expansion for eqn (35) is

$$u(x) = \beta - \frac{\ln\psi}{\beta} - \frac{(\ln\psi)^2}{2\beta^3} + \ldots \quad (36)$$

where $\beta = \sqrt{2\ln\nu_0 T}$. Substituting eqn (36) into the moment-based Hermite transformation model and retaining terms of $O(\beta^{-1})$ and greater, yields

$$g_{ng} = k\left\{\left(\beta + \frac{\gamma}{\beta}\right) + \hat{h}_3(\beta^2 + 2\lambda - 1) + \hat{h}_4 \times\left[\beta^3 + 3\beta(\gamma - 1) + \frac{3}{\beta}\left(\frac{\pi^2}{12} - \gamma + \frac{\gamma^2}{2}\right)\right]\right\} \quad (37)$$

where $\gamma = 0.5772$ (Euler's constant), $\beta = \sqrt{2\ln(\nu_0 T)}$ and ν_0 is the zero-upcrossing rate, k, $\hat{h}_3$, $\hat{h}_4$ are functions of skewness and kurtosis. For Gaussian processes, $\hat{h}_3$ and $\hat{h}_4 = 0$ and $\alpha = 1$ which reduces eqn (37) to the standard Gaussian form given by Davenport.[35] For the 900 s realization of data in Fig. 6, $\nu_0 = 1.334$. The peak factor based on eqn (37) using statistical information derived from the data is equal to -7.4, whereas the corresponding value for the Gaussian case is -3.9. It is important to note that eqn (37) is for positive extremes and for the negative extremes which we have considered here, the opposite of the skewness value must be used.

By comparison, Cheong[37] treats exceedence of a threshold which lies two standard deviations below the mean as a separate random variable. By choosing a low threshold, successive exceedences may be considered independent. The occurrence of exceedences of the threshold is modeled as a Poisson process and the distribution of exceedences is modeled by an exponential distribution. From this model, the distribution of the largest exceedence, S, for a duration, t, is derived as

$$P_S(t) = \mathrm{e}^{-\theta t e^{-\mu s}} \quad (38)$$

where μ and θ may be obtained from data as the reciprocals of the mean exceedence and the mean inter-exceedence interval, respectively. In terms of the distribution parameters, the expected value and the most probable value of the maximum exceedence are given by

$$E[S(t)] = \frac{\ln(\theta t) + 0.5772}{\mu} \qquad S_{mp} = \frac{\ln(\theta t)}{\mu} \quad (39)$$

Thus, the expected minimum C_p and its most probable minimum are

$$E[C_p(t)] = \bar{C}_p - 2\sigma_{C_p} - E[S(t)]$$
$$C_{p_{mp}} = \bar{C}_p - 2\sigma_{C_p} - S_{mp} \quad (40)$$

For the data considered above, $E[C_p(t)] = -7.019$, $C_{p_{mp}} = -6.562$. These values approach the peak factor attained by using the moment-based Hermite transformation model, but are somewhat less conservative in their estimate of the extreme value. This can be noted in Figs 6 and 7.

In a recent study, Krayer and Marshall[38] have pointed out that the linear gust factor based on extratropical storms may underestimate the gust factor for hurricane conditions. It is quite clear that the hurricane wind field comprised of turbulence due to convective processes superimposed upon a large, coherent vertical structure results in non-Gaussian fluctuations. Near the ground, a change in energy distribution with respect to frequency may result from non-linear interactions between different frequency components. Changes in the pdf and the power spectral density would certainly introduce changes in the statistics of velocity fluctuations, leading to a larger gust factor. A closer examination using a theory based on the preceding comments is being pursued to model the observed data.

SIMULATION OF NON-GAUSSIAN PROCESSES

Among a host of approximate analytical techniques developed for the analysis and prediction of non-linear system response, simulation methods are becoming more attractive due to the increasing ability of high speed computers. For implementation of time domain schemes, the time histories of loading functions are generated in accordance with desired statistical and spectral characteristics. The simulation procedures for Gaussian random processes are well established.[39–42] However, progress in the simulation of non-Gaussian processes has been elusive. A recent book on non-Gaussian processes provides an excellent overview of current methods of non-Gaussian simulation.[43] Several promising methods currently being pursued by the authors are presented here.

Correlation-distortion method

An approach used by Yamazaki and Shinozuka[44] for the simulation of non-Gaussian processes begins with the simulation of a Gaussian process which is then transformed to the desired non-Gaussian process through the following mapping:

$$X(t) = F_x^{-1}\{\phi(y)\} \tag{41}$$

An iterative procedure is necessary to match the desired target spectrum since the non-linear transformation in eqn (41) also modifies the spectral contents.

The necessity for an iterative procedure may be eliminated if one begins with the target spectrum or autocorrelation of the non-Gaussian process and transforms it to the underlying correlation of the Gaussian process.[45] Then, a simulation based on the schematic shown in Fig. 8 would eliminate the spectral distortion caused by the non-linear transformation. This approach is referred to as the correlation-distortion method in stochastic system literature.[46–48] For a given static single-valued non-linearity $x = g(u)$, where u is a standard normal Gaussian process, the desired autocorrelation of x in terms of y can be expressed as[47]

$$R_{uu}(\tau) = \sum_{k=0}^{\infty} a_k^2 \rho_{xx}^k(\tau)$$
$$a_k = \frac{1}{\sqrt{2\pi k!}} \int_{-\infty}^{\infty} g(\sigma u) \exp\left(-\frac{u^2}{2}\right) H_k(u)\mathrm{d}u \tag{42}$$

where ρ_{xx} is the normalized autocorrelation of the non-Gaussian process, and $H_k(u)$ is the kth Hermite polynomial given by

$$H_k(u) = (-1)^k \exp\left(\frac{u^2}{2}\right) \frac{\mathrm{d}^k}{\mathrm{d}u^k}\left[\exp\left(-\frac{u^2}{2}\right)\right] \tag{43}$$

An alternative to the preceding approach is to express x as a function of a polynomial whose coefficients are determined by a minimization procedure (e.g. Ref. 49). Another approach uses translational models involving the Hermite moment transformation described earlier. In this study, we utilize a Hermite model. The simulation algorithm is as follows: (i) estimate the auto-correlation of the mean-removed normalized parent non-Gaussian process to be simulated; (ii) transform to the auto-correlation of the underlying Gaussian process by solving

$$R_{xx}(\tau) = \alpha^2[R_{uu}(\tau) + 2\hat{h}_3^2 R_{uu}^2(\tau) + 6\hat{h}_4^2 R_{uu}^3(\tau)] \tag{44}$$

for $R_{uu}(\tau)^{24}$, where eqn (44) is a truncated infinite series, and the unspecified parameters are defined in eqn (16); (iii) simulate a Gaussian process using the spectrum associated with $R_{uu}(\tau)$; (iv) transform this process back to a non-Gaussian process using

$$x = \alpha[u + \hat{h}_3(u^2 - 1) + \hat{h}_4(u^3 - 3u)] \tag{45}$$

(v) replace the mean and variance of the original parent process. A sample realization of a simulated process consistent with the data in Fig. 6 is given in Fig. 9. The comparison of simulated and target pdfs and spectral characteristics is excellent and is shown in Fig. 10, where the simulation results are an ensemble average of 100 realizations.

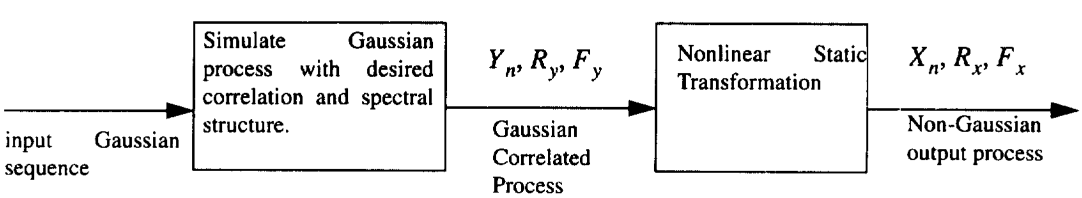

Fig. 8. Schematic of the correlation-distortion method of non-Gaussian process simulation.

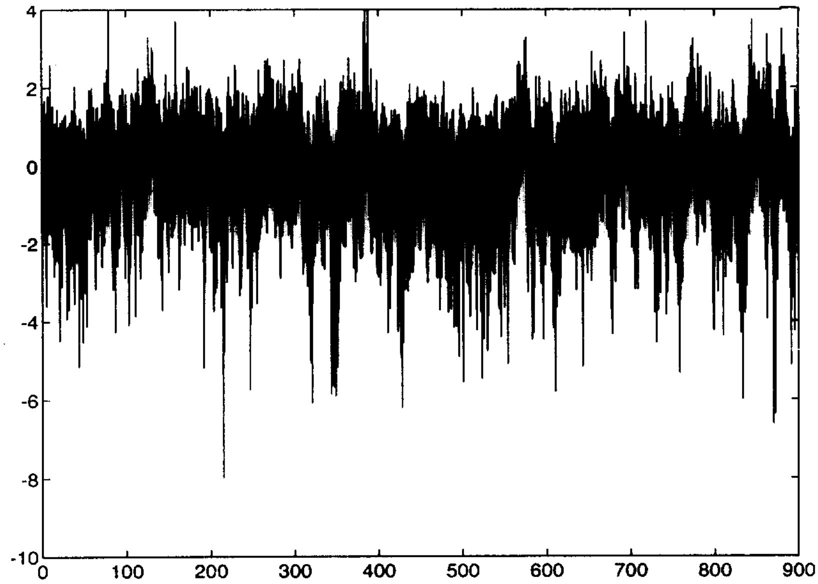

Fig. 9. Sample realization of simulated pressure data in Fig. 7 using correlation-distortion.

Direct transformation methods

Another application of the correlation-based approach concerns the simulation of a process consistent with a sample of a non-Gaussian time history. The non-Gaussian sample process, $x(t)$, is transformed to its Gaussian underlying form, $u(x)$, through eqn (16). Subsequently, linear simulations created through standard techniques based on the target spectrum of the Gaussian process are transformed back to the non-Gaussian parent form through eqn (45). The shortcoming of this direct transformation technique is the distortion of the frequency distribution of signal energy. The resulting simulated non-Gaussian signal power spectrum does not match the parent non-Gaussian spectrum to a satisfactory degree. This distortion may stem from the inability of the three-term truncated Hermite moment transformation in eqn (16) to produce a Gaussian signal for cases when the parent signal is highly non-Gaussian. The linear simulation is then based on a target spectrum derived from a process which is assumed Gaussian, but is not. It is at this point where the frequency information is distorted, and results in poor simulations. One option for improved results is to add terms to the Hermite series until a Gaussian transformation is achieved. This may require a different number of terms to achieve accuracy for varying input sample signals.

A simple correction has been suggested to remove this distortion in the direct transformation method.[45]

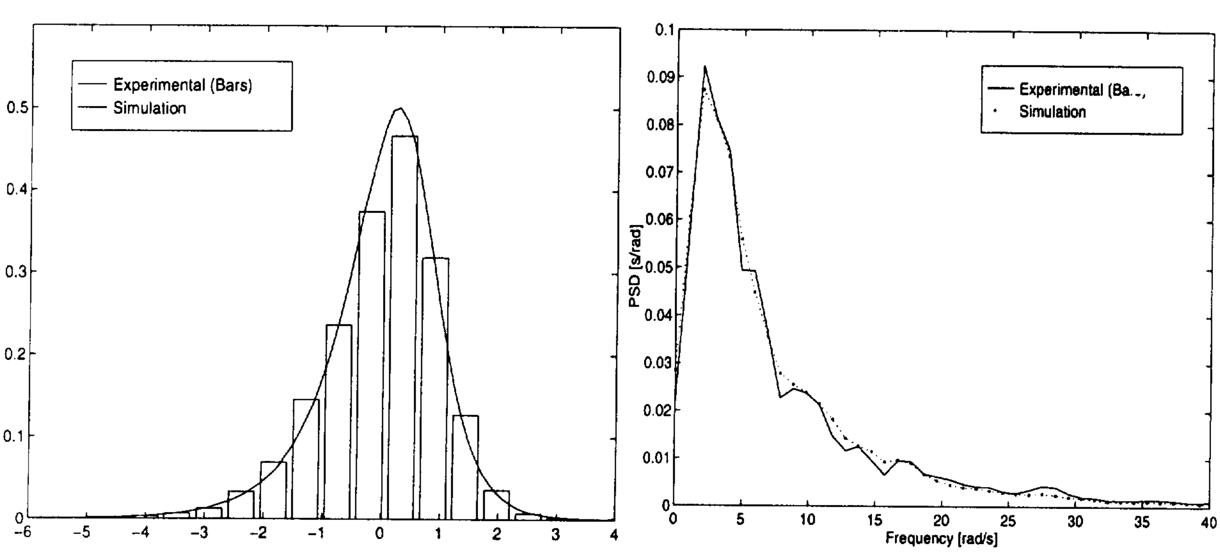

Fig. 10. Pdf and power spectral density of measured and ensemble of simulated records using correlation-distortion method.

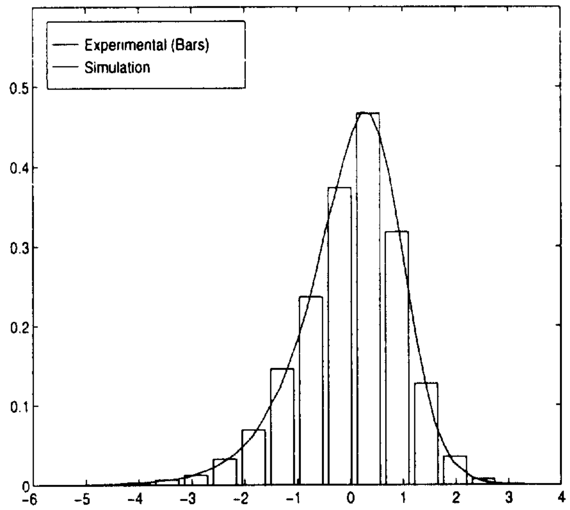

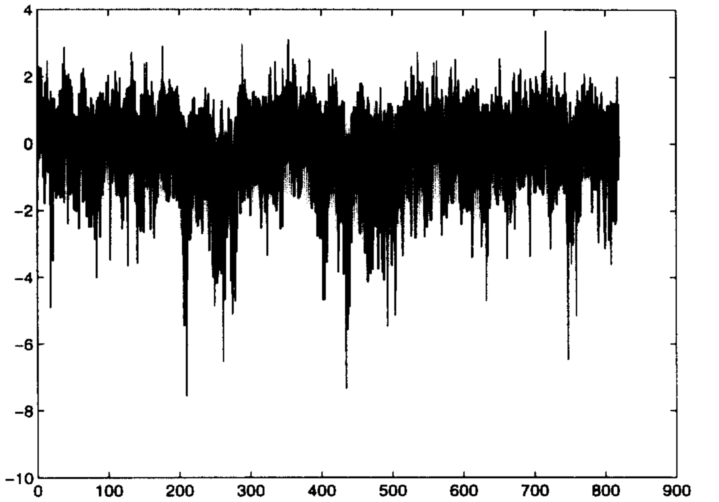

Fig. 11. Pdf of measured and ensemble of simulated records and a realization of the pressure record in Fig. 6 using modified direct transformation method.

Referring to eqn (16), it can be seen that the governing parameters $\hat{h}_3$, $\hat{h}_4$, a, b, c, α and thus $u(x)$ are dependent on the skewness and kurtosis. γ_3 and γ_4 may be treated as adjustable input parameters in order to force the transformed process, $u(x)$, to be Gaussian. Optimization of these two parameters is based on the minimization of the function

$$\min(\gamma_{4_u}^2 + \gamma_{3_u}^2) \tag{46}$$

where γ_{3_u} and γ_{4_u} are the skewness and kurtosis of the inverse Hermite transformed process $u(x)$. The optimized input parameters γ_3 and γ_4 now provide a Gaussian process, and the linear simulations do not contain distortion. The same parameters are used to transform back to a non-Gaussian simulation whose pdf and power spectral density closely match those of the parent process. This correction is essentially a quantification of the error in truncating the Hermite series after the third order.

An example is given in Fig. 11, where the simulated and target pdf are shown along with a sample realization of the measured pressure in Fig. 6. The pdf is an ensemble average of the pdfs from 100 realizations of the same length as the original record. The comparison of target and simulation power spectral density is similar to that in Fig. 10, and is not shown here.

Simulation based on higher-order transfer functions

The Volterra series model in the frequency domain (eqn (2)) lends itself to the simulation of non-linear processes for which the Volterra kernels are available or may be estimated. A second-order non-Gaussian signal resulting from a quadratic transformation of a Gaussian process may be simulated by the addition of second-order contributions to the complex spectral amplitude components at the appropriate sum and difference frequencies before inverse Fourier transforming the sequence to the time domain. These second-order contributions are formed from the products of pairs of linear Fourier components with the QTF in the frequency domain, and correlate the phase between various frequency components to a degree weighted by the QTF. The memory retained by convolution with the QTF facilitates the simulation of processes that are able to match not only the power spectrum and pdf of the parent process, but the bispectrum as well.

This approach requires information concerning the QTF of the desired process. In the case of non-Gaussian waves and their loads on offshore structures, the QTFs can be derived computationally. However, in the case of wind effects this is not possible due to the complexity of non-linear interactions that take place as turbulent wind encounters a structure. In the absence of the necessary information, it is possible to estimate a QTF based on the desired process and an extracted underlying Gaussian process. Such an attempt is made here by using the pressure data in Fig. 6. Due to the presence of higher-order non-linearities, an estimated QTF may not completely model the non-Gaussian features. This concept in principle may easily be extended to the simulation of non-linear processes beyond the second order, where higher-order information, e.g. trispectrum, may improve the model.

A simulation based on a QTF extracted from pressure data is shown in Fig. 12, along with a sample of the measured data, and indeed reflects a lack of completeness in the second-order Volterra model. The model fails to properly reflect the skewness and kurtosis of the measured record. The use of higher-order transfer functions is currently being researched to improve upon the simulation. A second example is shown in Fig. 13, where the data being simulated is mean-removed

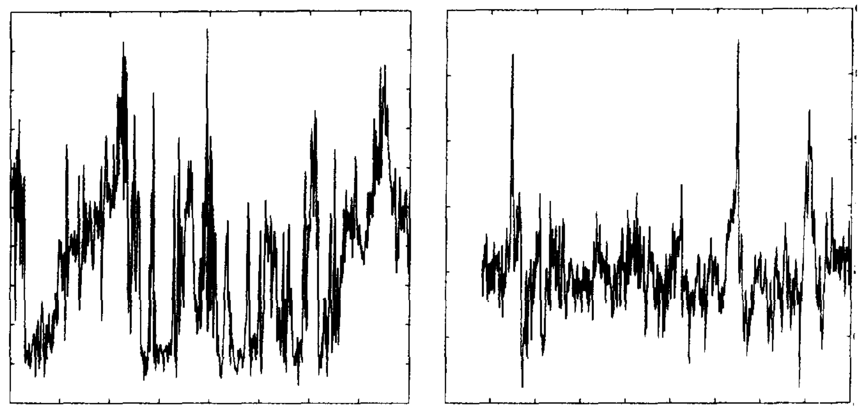

Fig. 12. Non-Gaussian simulated pressure realization using eqn (2) (left), and a measured sample of pressure data (right).

measured wind velocity from a hurricane. In this case the higher-order statistics of the measured and simulated processes match up well, and the visual comparison is much closer to the target than the previous example. The second-order Volterra model is appropriate for the severity and type of non-linearity in this case.

The role of phase tailoring

It is also interesting to examine the role of phase tailoring. It will be shown here that certain constraints on the envelope of the time series may be accommodated by controlling the phase. The widely used simulation approach for generating processes with a prescribed spectral density function uses the inverse Fourier transform of a complex amplitude spectrum whose components possess deterministically chosen amplitudes and random phases. For a phase angle of zero, the simulated time history represents the impulse response of a system. For a linearly varying phase spectrum, the resulting time series is the same as a delayed zero phase. Accordingly, a random phase results in a random signal. This is in direct contrast to the distinctly transient, impulse response-like signal which is generated when smooth and deterministic phase variation with frequency is introduced.[50] An assumed description of the phase spectrum does not alter the spectral characteristics of the simulated time history. It is thus possible to introduce spiky features or grouping effects in a simulated time history by tailoring the phase spectrum before inverse Fourier transformation. Such deterministic signals cannot be utilized for statistical analysis, but may be quite useful for deterministic applications such as input to a system under test loading. The importance of phase information in the Fourier representation of non-Gaussian pressure records is used as the basis for a simulation method which combines an autoregressive model with Fourier transformation.[51] Kobayashi *et al.*[52] have implemented the concept of phase tailoring in a wind-tunnel simulation of wind gusts observed at a site utilizing oscillating vanes.

The phase spectrum contains no relevant information under the assumption of a Gaussian random process. However, attention has recently been given to the identification of phase information for non-Gaussian processes. Bispectral analysis of measured processes, e.g. ocean wave records, indicates the presence of phase coupling among the various component wave frequencies in many cases. This coupling results in a non-Gaussian signal which is capable of dramatically altering the response statistics of a system thought to be subject to Gaussian input. The removal of the coupled phase information from the record returns a Gaussian signal with no significant bispectral characteristics, but identical autospectra. This demonstrates the potential importance of the phase information in

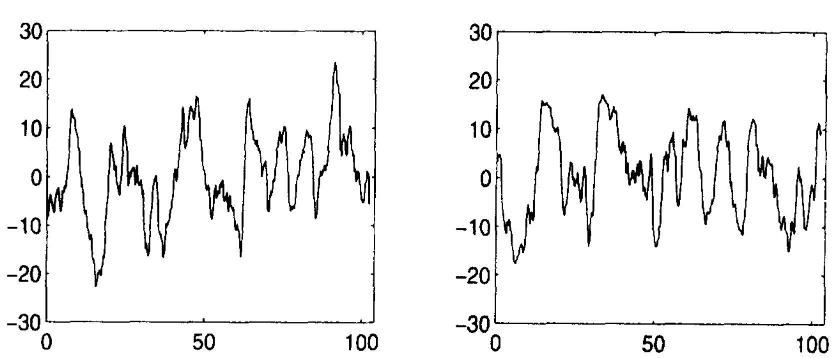

Fig. 13. Non-Gaussian simulated hurricane wind velocity realization using eqn (2) (left), and a measured sample of hurricane wind velocity data (right).

identifying non-Gaussian signals, and is the basis of the simulation of non-Gaussian signals in the previous section, where the second-order contributions to the linear complex spectral amplitudes result in phase coupling weighted by QTF. The interpretation of information from the phase spectrum of non-Gaussian signals is still not well established and is an area of current research in wave mechanics, e.g. Ref. 52. Higher-order spectral analysis offers a convenient format which has provided significant insight into phase information, and is currently being used as a tool to identify distinctive phase characteristics of non-Gaussian wind pressure data.

In a less complicated application of phase tailoring, the injection of constant phase over a small frequency range of otherwise random phase results in a signal with characteristics often desired in the simulation and analysis of system response to particular types of grouped input. This concept may be applied to simulating concentrated groups of turbulent gusts during a thunderstorm in synthetic wind records. Further work is needed to identify and quantify the existence of such groups of gusts in thunderstorms.

Conditional simulation

Simulation of random velocity and pressure signals at uninstrumented locations of a structure conditioned on measured records are often needed in wind engineering. For example, malfunctioning instruments may leave a hole in a data set or information may be lacking due to a limited number of sensors. This concept is similar to conditional sampling in experiments or numerical simulations. This field has matured significantly in the last few years (e.g. Refs 54–58). Fundamentally, two approaches have been introduced in which the simulation is either based on a linear estimation or kriging, or on a conditional probability density function. Following Borgman's work on ocean waves,[54] Murlidharan and Kareem[59] have developed schemes for conditional simulation of Gaussian wind fields utilizing both frequency and time domain conditioning. The conditional simulation permits generation of time histories at new locations when one or more time series for the full length interval are given, and extension of existing records beyond the sampling time for cases where conditioning time series are limited to a small subinterval of the full length. Consider a pair of correlated Gaussian random vectors V_1 and V_2. Let the bivariate normal distribution of these variables be denoted

$$p(V) = p\begin{bmatrix} V_1 \\ V_2 \end{bmatrix} = N\left(\begin{bmatrix} \mu_1 \\ \mu_2 \end{bmatrix}, \begin{bmatrix} C_{11} & C_{12} \\ C_{21} & C_{22} \end{bmatrix}\right) \tag{47}$$

where μ_1 is the mean value, and C_{ij} is the auto or cross-covariance between the variables. If a sample of V_1 is measured and denoted as v_1, then it is the conditional simulation of V_2 based on the measured record that is desired. The conditional pdf for V_2 given the information on V_1 is expressed as

$$p(V_2 | V_1 = v_1) = N(\mu_2 + C_{12}^{\mathrm{T}} C_{11}^{-1}(v_1 - \mu_1), C_{22} - C_{12}^{\mathrm{T}} C_{11}^{-1} C_{12}) \tag{48}$$

and a conditional simulation is provided by

$$(V_2 | V_1 = v_1) = C_{12}^{\mathrm{T}} C_{11}^{-1}(v_1 - V_1) + V_2 \tag{49}$$

Derivations of the covariance matrices C_{11} and C_{12} in the time and frequency domains then provide all that is needed for conditional simulation. Details concerning these matrices for wind simulation may be found in Murlidharan and Kareem.[59] In a conditionally simulated field, fluctuations at intermediate points will follow the fluctuations of the surrounding locations provided the scale of fluctuations at surrounding locations. An interesting application of conditional simulation concerns generation of wind velocity fluctuation at a large number of grid points as an upwind boundary condition for a computational study conditioned on measurements at a limited number of locations in a wind tunnel.[60]

An example application of Gaussian conditional simulation is shown in Figs 14 and 17. These examples are based on measured correlated wind velocity records at four elevations on a full-scale tower with the mean removed. Figure 14 shows three of these records at stations 1 through 3 and a frequency domain conditional simulation of the fourth location based on information from the other three known records. Here, eqn (49) is used for a uni-dimensional multivariate conditional simulation. Figure 15 is a comparison of the target cospectrum with the cospectrum between the measured records at station 1 and 4, and the cospectrum between the conditionally simulated record at station 4 and the measured record at station 1. The jaggedness of the cospectra in the figure arises from the variance inherent in individual realizations. An ensemble average of many simulations results in a smooth cospectrum which lies along the target cospectrum. Figure 16 is a comparison of the target power spectral density with that from the measured and conditionally simulated records at station 4. Figure 17 shows a measured record up to 2500 s in the top figure. It is assumed here that the record is only available up to 980 s, indicated by the darker portion of the signal. A time domain conditional simulation of the record from 980–2500 s is shown as the lighter portion in the bottom figure, based on information from the first 980 s. The lighter part of the top figure indicates the portion of this signal which is not known when generating the bottom figure. Both examples demonstrate the effectiveness and utility of conditional simulation.

In cases involving non-Gaussian processes, the conditional simulation schemes suffer impediments like their Gaussian counterparts. In Elishakoff *et al.*,[58]

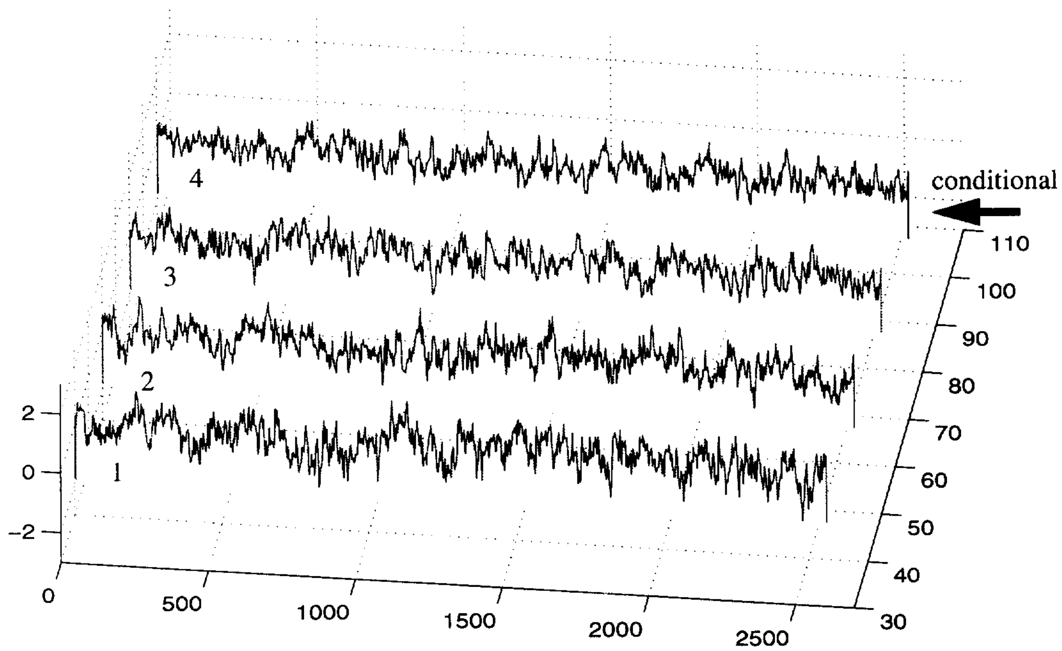

Fig. 14. Measured wind velocity at 40, 60 and 80 m, frequency domain conditional simulation at 100 m based on records at lower three stations.

iterative schemes have been utilized to simulate non-Gaussian processes. The authors sought to combine the techniques developed for unconditional simulation of non-Gaussian processes and the procedure of conditional Gaussian processes. The non-Gaussian known processes are mapped into underlying Gaussian processes, where conditional simulation is done. These simulated time histories are then mapped back into the non-Gaussian domain.

WAVELET TRANSFORMS

The inability of conventional Fourier analysis to preserve the time dependence and describe the evolutionary spectral characteristics of non-stationary processes requires tools which allow time and frequency localization beyond customary Fourier analysis. The short-term Fourier transform (STFT) provides time and frequency localization to establish a local spectrum for

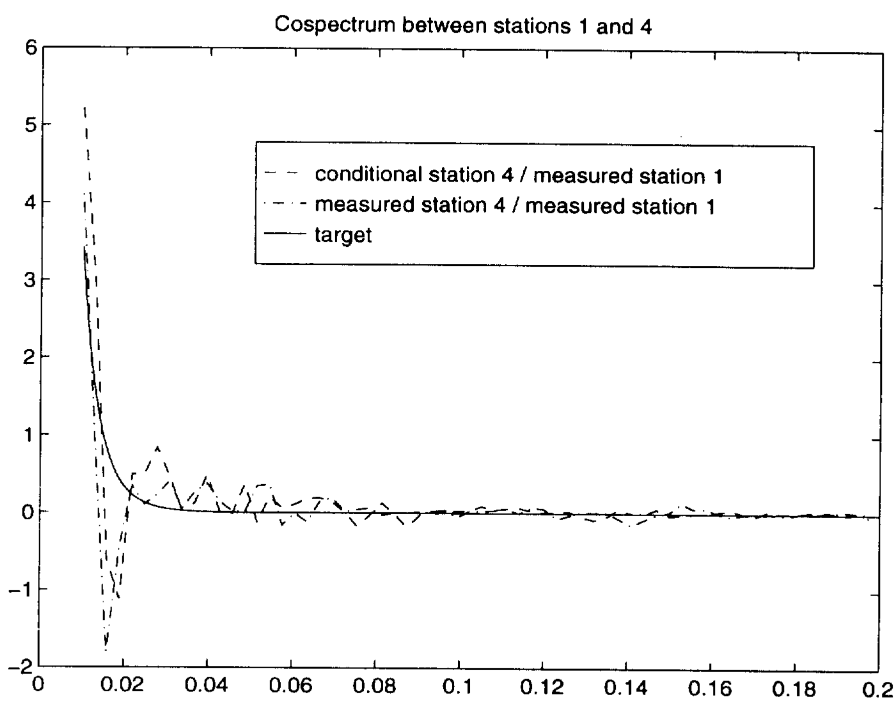

Fig. 15. Conditional, measured, and target cospectral density between stations 1 and 4.

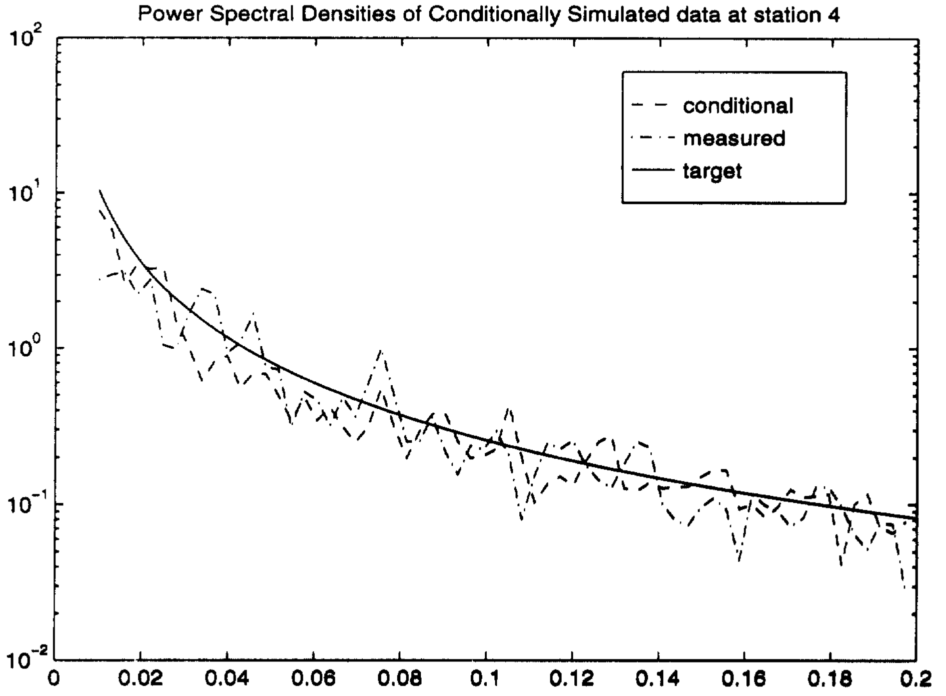

Fig. 16. Target, measured, and conditionally simulated power spectral density at station 4.

any time instant. The problem is that high resolution cannot be obtained in both time and frequency domains simultaneously. The moving window must be chosen for locating sharp peaks or low frequency features, because of the inverse relation between window length and the corresponding frequency bandwidth.

This drawback can be alleviated if one has the flexibility to allow the resolution in time and frequency to vary in the time–frequency plane to reach a multi-resolution representation of the process. This is possible if the analysis is viewed as a filter bank consisting of band-pass filters with constant relative bandwidths. One type of local transform is the recently developed wavelet transform (WT) which decomposes a signal using

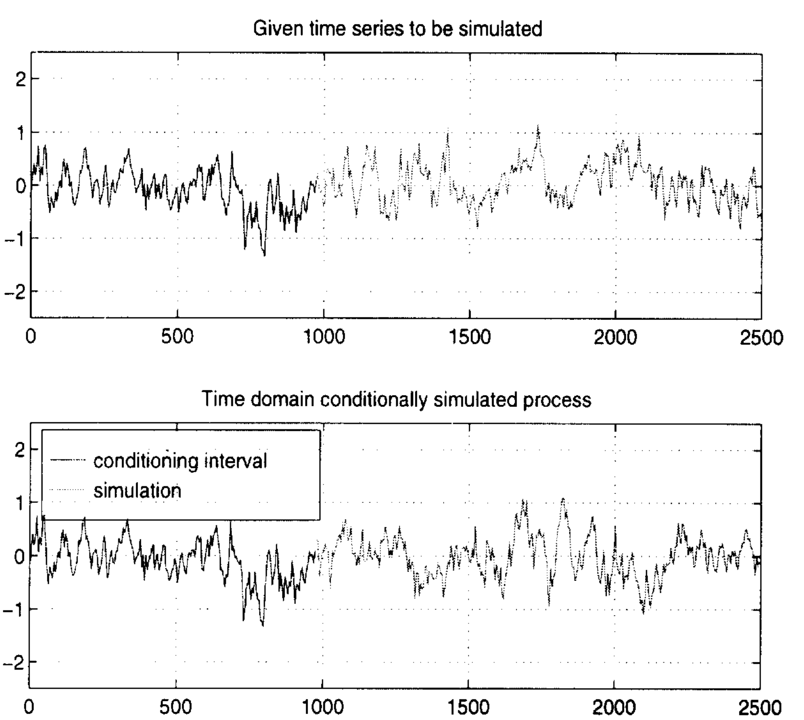

Fig. 17. Measured wind velocity (top figure) and time domain conditional simulation (light portion of bottom figure).

wavelet functions. Fourier methods of signal decomposition use infinite sines and cosines as basis functions, whereas the wavelet transform uses a set of orthogonal basis functions which are local. Various dilations and translations of a parent wavelet are joined to form the family of basis functions. This allows the retention of local transient signal characteristics beyond the capabilities of the harmonic basis functions. The wavelet transform allows a multi-resolution representation of a process and provides a flexible time–frequency window which narrows to observe high frequency energy content, and broadens to capture low frequency phenomena.

Brief wavelet overview

Development of the parent wavelet begins with the solution of a dilation equation to determine a scaling function $\phi(n)$, dependent on certain restrictions. The scaling function is used to define the parent wavelet function, $\psi(n)$. The basis functions used to represent the signal are defined by translations and dilations of the parent wavelet. The shape of the parent wavelet is not a single unique shape, but depends on the desired wavelet order.

The signal being decomposed must consist of 2^M samples, where M is an integer. Wavelet analysis decomposes the signal into $M+1$ levels, where the level is denoted as i, and the levels are numbered $i = 1, 0, 1, \ldots, M-1$. Each level of i consists of $j = 2^i$ translated and partially overlapping wavelets equally spaced $2^M/j$ intervals apart. The $j = 2^i$ wavelets at level i are dilated such that an individual wavelet spans $N-1$ of that levels intervals, where N is the order of the wavelet being applied. Each of the $j = 2^i$ wavelets at level i is scaled by a coefficient $a_{i,j}$ determined by the forward wavelet transform, a convolution of the signal with the wavelet. The notation is such that i corresponds to the wavelet dilation, and j is the wavelet translation in level i. $a_{i,j}$ is often written as a vector a_{2^i+j}, where $j = 0, 1, \ldots, i-1$. There are as many wavelet coefficients as signal samples. The level $i = -1$ is the signal mean value.[61] A variety of packages are available to perform discrete wavelet transform (DWT) analysis (e.g. Ref. 62).

Applications to wind engineering

The present research concerns the use of wavelets to aid in the analysis and simulation of non-stationary data. Multi-scale decomposition of processes utilizing wavelets reveals events otherwise hidden in the original time history. Wavelet coefficients may be used to derive an estimate of the power spectrum. These estimates may be extended to multi-variate, e.g. cospectral, estimation. The wavelet coefficients provide the scalogram, which describes the signal energy on a time-scale domain over a range of logarithmically-spaced frequency bands. This facilitates identification of time-varying energy flux and spectral evolution. The property of accurate energy representation lends itself well to signal reconstruction and simulation. A stochastic manipulation of the wavelet coefficients leads to a simulation which is statistically similar to the original signal.

Wavelet filterbank

Figure 18 presents the time history of the response of a large floating structure to wind and wave loads, and the resulting band-passed time histories using a wavelet-based filterbank. The summation of the band-passed histories returns the original time history. This figure unfolds the response time history into a very revealing display of the time-scale representation. The top left block is the mean-removed original signal, the blocks following column-wise downward are the band-pass filtered signal in order of decreasing frequency, and the lower right block is the low pass channel or mean of the signal. Note the different scales on the plots for the filtered processes, indicating relative contribution in that frequency band. The power spectral density of the signal in Fig. 18 is shown in Fig. 19, in which the frequency bands 1 through 7 of the filtered process are marked. The higher relative magnitudes of bands 3 and 4 correspond to the right peak in the spectrum, and are due to first-order wave effects. The high relative magnitude in bands 6 and 7 corresponds to structural resonance due to wind and second-order wave effects. The wavelet-based filter bank has helped to identify, e.g. high frequency spikes and their time of occurrence, associated with waves slamming the structure, observed in bands 1 and 2. These transient events in the response of the structure exposed to wind and wave fields are not clearly discernible in the time history where large excursions may be due to either occasional slamming, or large but not slamming waves. The improved efficiency over FFT and other filtering techniques, e.g. multi-filtering with simple oscillators (e.g. Ref. 63), renders wavelet filterbanks a quick and convenient time-scale decomposition method.

Signal analysis with spectral methods and wavelets/time-scale decomposition

A wavelet power spectrum is estimated by plotting the summed coefficients with respect to the scale axis only. Small changes in frequency within an octave band are not easily resolvable. This is a larger problem for the high frequency range where the octave spans half the total frequency range. This may be alleviated by several methods which allow intra-octave wavelet coefficient estimation. One option is to apply a number of slightly dilated parent wavelets recursively to the data, creating a denser sampling grid than the octave-by-octave grid used by the original parent wavelet.[64] Another method

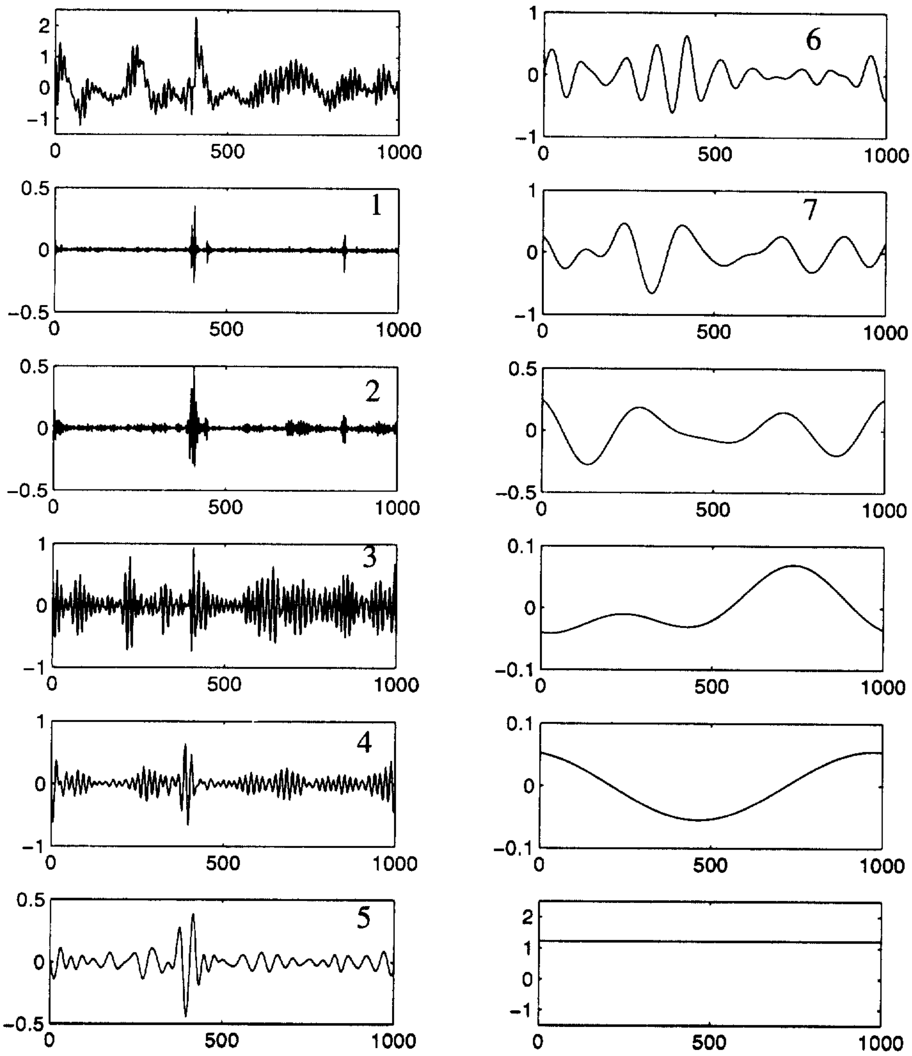

Fig. 18. From left column-wise downward: measured offshore structured response to wind and wave field and its time-scale decomposition using wavelet transforms.

used in this study is the application of zoom techniques to the filtered data.

An example of octave band and intra-octave band wavelet spectral estimations and an FFT-based estimation are shown in Fig. 20. The left figure is the power spectrum of the response of an offshore platform to wind loads, and the right figure is the cospectrum between the measured wind speed input and resulting platform response. The areas under the wavelet spectral and cospectral estimates represent the true variance and covariance from the time histories almost exactly, while the area under the FFT estimate does not. Further, smoothing of the FFT estimate with segment averaging renders its resolution inferior to that of the wavelet estimate at low frequencies. The FFT spectral estimates are the average of eight segments, while the wavelet estimate is based on the entire data record.

Wavelength coefficients in an octave band represent the energy at time intervals equally spaced over the duration of the signal, and may be used to analyze non-stationary events for transient and evolutionary phenomena. Accordingly, the transfer of energy from one octave band to the next may be observed along the time-scale in the scalogram. Two example applications of the scalogram are shown in Figs 21 and 22. In Fig. 21 the analyzed signal in the top plot is a sine wave of constant amplitude whose frequency is steadily increased in time. The transfer of energy from lower to higher frequencies in time is clearly demonstrated as the dark region. In Fig. 22, the signal is a hurricane velocity record measured after the hurricane eye has passed the instrument. In the scalogram the light region shows the band of frequency content of the record remains relatively constant, while the magnitude at earlier times is larger than at later time, suggesting non-stationary features.

Wavelet simulation of non-stationary processes

The concept of applying a modulated stationary process centred at narrow-banded frequencies to model ground motion has been extensively used (e.g. Refs 65, 66). In

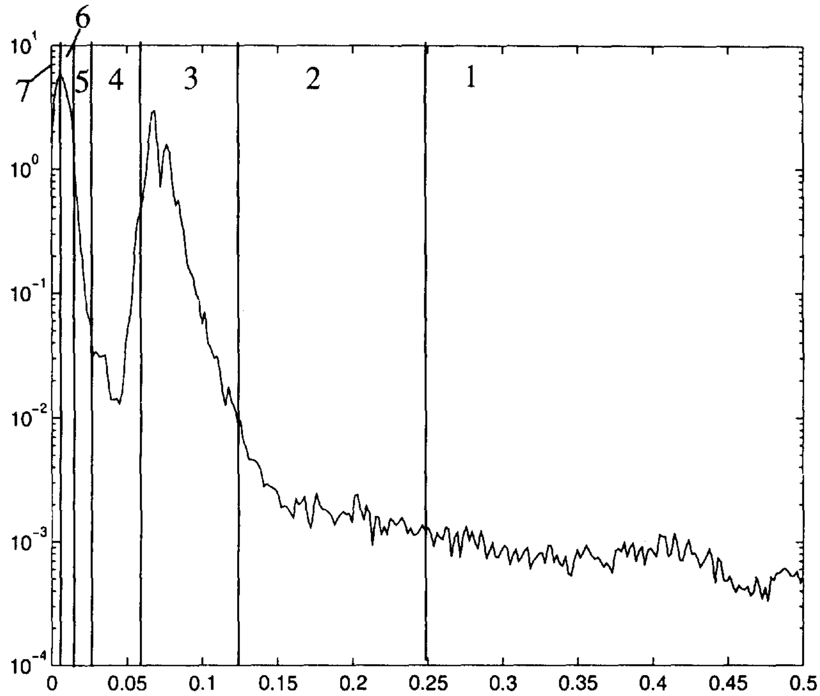

Fig. 19. Power spectral density of measured offshore structural response seen in Fig. 18.

this representation each component process, $s_j(t)$, is modulated by a different modulating function $m_j(t)$

$$x(t) = \sum_j m_j(t)s_j(t) \tag{50}$$

There are different approaches to modeling m_j and s_j to describe x.

The retention of both time and frequency information makes wavelets a useful tool for the simulation of non-stationary signals. This can be done given either a parent non-stationary signal, or a target spectrum and modulation function for each octave. Given a parent non-stationary signal, e.g. a local wind velocity record, an ensemble of signals may be simulated whose average statistics closely resemble those of the parent process. The parent signal is discrete wavelet transformed (DWT), and the coefficients multiplied by a Gaussian white noise of unit variance $w(n)$. The inverse wavelet transform (IWT) then produces a simulation statistically similar to the parent process.

Given a target spectrum and modulator functions for each octave, the simulation is done by first finding the

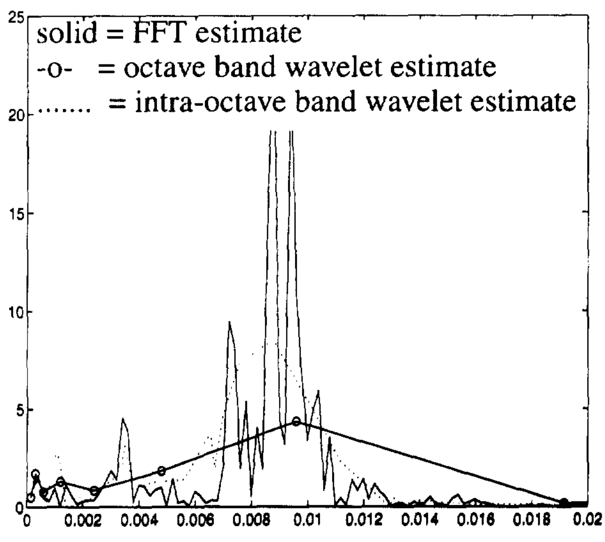

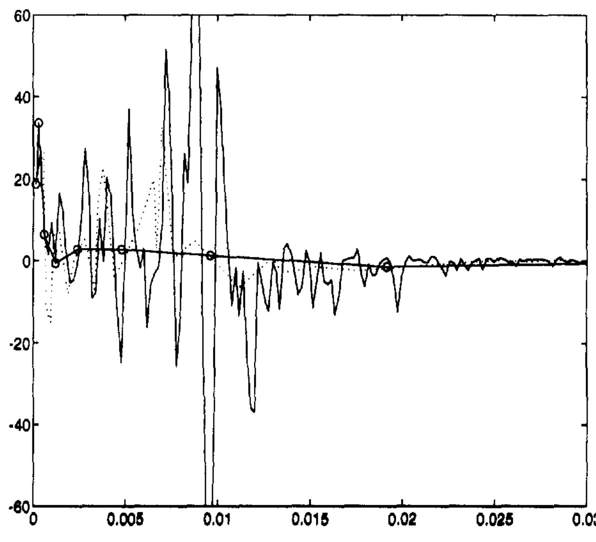

Fig. 20. Left — Power spectrum estimates of offshore platform response using FFT, octave band wavelet, and intra-octave band wavelet estimation techniques. Right — cospectrum estimates between wind velocity input and resulting platform response.

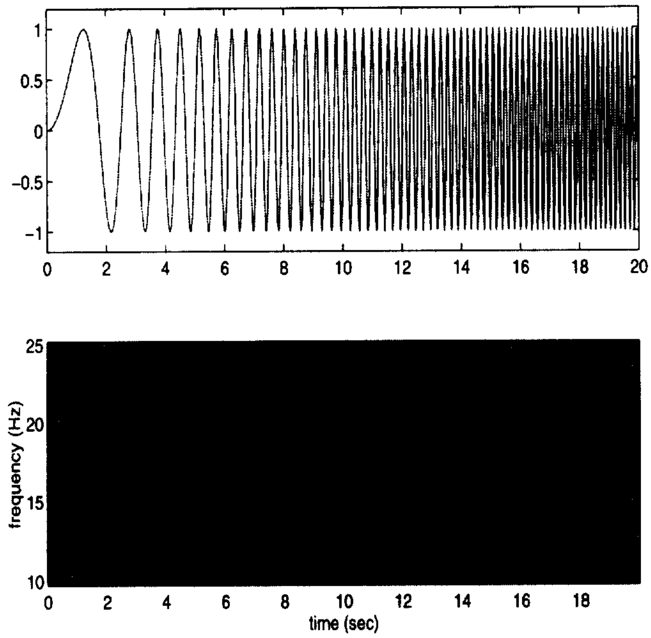

Fig. 21. Frequency modulated sine wave and scalogram.

energy contained in each octave from the target spectrum. The wavelet coefficients for the simulated process are multiplied with the appropriate modulator, and normalized such that the energy equals that in the corresponding octave. These modulated and normalized coefficients are then multiplied through by white noise and inverse wavelet transformed. The process is represented by[67]

$$\hat{x}(n) = IWT\left(w(n)^*\left(\frac{m_{ij}\sqrt{S_i}}{\sqrt{2^{i+2-M}}}\right)\right) \tag{51}$$

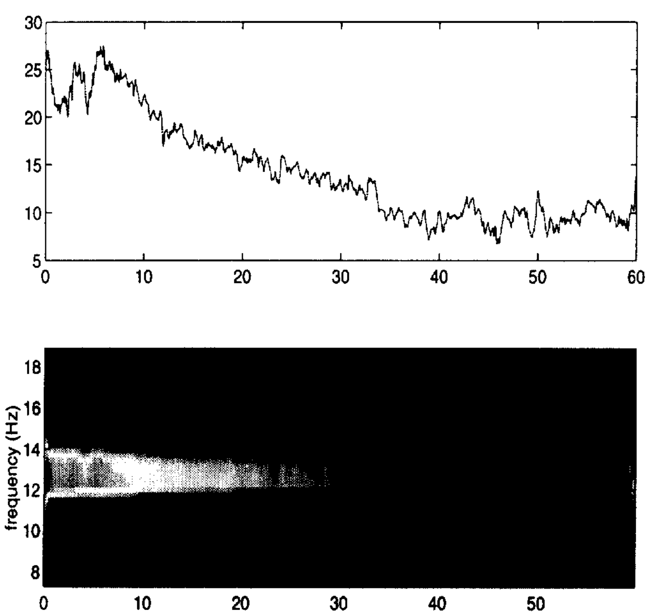

Fig. 22. Measured hurricane data and scalogram.

When a parent signal is used to determine the modulator function, the measured wavelet coefficients $a_{i,j}$ and target spectrum are used as

$$m_{i,j} = A_i\sqrt{2^{i+2-M}}\frac{|a_{i,j}|}{\sqrt{S_i}} \tag{52}$$

where A_i is the level-dependent amplitude constant and S_i is the energy corresponding to the ith octave from the target power spectrum. Figure 23 shows a measured non-stationary wind velocity record, and a simulated process using the wavelet transform. Both statistical and visual comparisons between the target and simulated records are good.

CONCLUDING REMARKS

Progress in quantifying and simulating the non-Gaussian and non-stationary effects of wind on structures has been elusive due to the limitations of traditional analytical tools. Here, an overview of techniques is presented with examples which aid in the efficient modeling, simulation, and pdf estimation of non-Gaussian processes. The estimation of Volterra kernels from system identification is addressed, as well as other representations for non-linear systems. The estimated pdf of non-linear system response is presented via several methods with examples which involve the use of Volterra kernels in the Kac–Siegert approach, the use of joint moment information as constraints on system entropy, and the use of moment-based Hermite transformation models. Several techniques for simulating non-Gaussian signals, including convolving Fourier amplitude pairs with higher-order Volterra kernels, non-linear mapping, as well as the concept of conditional

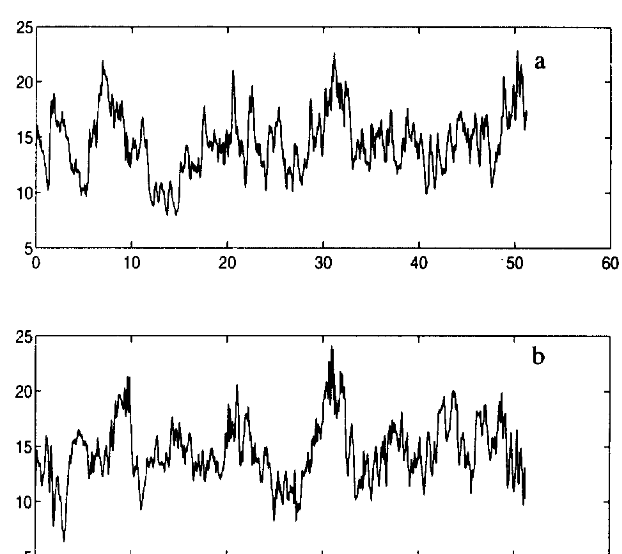

Fig. 23. (a) Measured and (b) a realization of simulated wind velocity using wavelet transform.

simulation, are discussed. The implications of non-Gaussian winds and their load effects on fatigue damage and gust factor representation of dynamic wind loads are illustrated. The analysis and simulation of non-stationary processes is accomplished by the application of localized basis functions via the wavelet transform. Applications and examples are given which pertain to non-stationary effects of wind on structures.

ACKNOWLEDGEMENTS

The support for this work was provided in part by NSF Grants BCS-9096274 (BCS-8352223), CMS9402196, and ONR Grant N00014-93-1-0761. The first and second authors were partially supported by a Department of Education GAANN Fellowship during this study.

REFERENCES

1 Peterka, J. A. and Cermak, J. E. Wind pressures on buildings — probability densities. *J. Structural Div., ASCE*, 1973, **101**(ST6), 1255–1267.
2. Kareem, A. Wind excited motion of tall buildings. PhD. dissertation in partial fulfillment of the degree of doctor of philosophy, Colorado State University, Fort Collins, Co, 1978.
3. Kareem, A., Hsieh, C. C. and Tognarelli, M. A. Response analysis of offshore systems to nonlinear random waves part I: wave field characteristics. *Proc. Special Symp. on Stochastic Dynamics and Reliability of Nonlinear Ocean Systems*, eds Ibrahim and Lin. ASME, Chicago, IL, 1994.
4. Holmes, J. D. Non-Gaussian characteristics of wind pressure fluctuations. *J. Wind Engng and Ind. Aerodyn.*, 1981, **7**, 103–108.
5. Kawai, H. Pressure fluctuations on square prisms-applicability of strip and quasi-steady theories. *J. Wind Eng. Aerodyn.*, 1983, **13**, 197–208.
6. Letchford, C. W., Iverson, R. E. and McDonald, J. R. The application of the quasi-steady theory to full scale measurements on the Texas tech building. *J. Wind Engng and Ind. Aerodyn.*, 1993, **48**, 111–132.
7. Thomas, G., Sarkar, P. P. and Mehta, K. C. Identification of admittance functions for wind pressures from full-scale measurements. *Proc. Ninth Int. conf. on Wind Engineering*, New Delhi, India, 9–13 January, pp. 1219–1230.
8. Tieleman, H. W. and Hajj, M. R. Pressures on a flat roof-application of quasi-steady theory. *Proc. ASCE Specialty Conf., Engineering Mechanics*, Boulder, CO, 1995.
9. Davenport, A. G. Note on the distribution of the largest value of a random function with application to gust loading. *Proc. Institution of Civil Engineers London*, **28**, 1964, pp.187–196.
10. Schetzen, M. *The Volterra and Wiener Theories of Nonlinear Systems*. John Wiley and Sons, New York, 1980.
11. Kareem, A. and Li, Y. On modeling the nonlinear relationship between random fields by means of higher-order spectra. *Probalistic Methods in Civil Engineering*, ed. P. D. Spanos. ASCE, NY, 1980, pp. 384–387.
12. Spanos P. D. and Donley, M. G. Equivalent statistical quadratization for nonlinear systems. *J. Engng Mech., ASCE*, 1991, **117**(6), 1289–1309.
13. Kareem, A. and Zhao, J. Analysis of non-Gaussian surge response of tension leg platforms under wind loads. *J. Offshore Mech. and Arctic Engng, ASME*, 1994, **116**, 137–144.
14. Nam, S. W., Powers, E. J. and Kim, S. B. Applications of digital polyspectral analysis of nonlinear system identificatin. *Proc. 2nd IASTED Int. Symp. of Signal Processing and its Applications*. Gold Coast, Australia, pp. 133–136, 1990.
15. Bendat, J. S. *Non-linear System Analysis and Identification from Random Data*. John Wiley and Sons, Inc., New York, 1990.
16. Kung, S. Y. *Digital Neural Networks*. Prentice Hall, Englewood Cliffs, NJ, 1993.
17. Hertz, J., Krogh, A. and Palmer, R. G. *Introduction to the Theory of Neural Computation*. Addison-Wesley Publishing Company, New York, 1991.
18. Antsaklis, P. J. Control theory approach. *Mathematical Approaches to Neural Networks*, ed. J. G. Taylor. Elsevier Science Publishers B.V., 1993, pp. 1–23.
19. Ochi, M. K. Non-Gaussian random processes in ocean engineering. *Probabilistic Engng Mech.*, 1986, **1**, 28–39.
20. Calderone, I., Cheung, J. C. K. and Melbourne, W. H. The full-scale significance, on glass cladding panels, of data obtained from wind tunnel measurements of pressure fluctuations on building cladding. *J. Wind Engng and Ind. Aerodyn.*, 1994, **53**, 247–259.
21. Sobczyk, K. and Trebicki, J. Maximum entropy principle in stochastic dynamics. *Probabilistic Engng Mech.*, 1990, **5**(3), 102–110.
22. Kapur, J. N. *Maximum Entropy Models in Science and Engineering*. John Wiley and Sons, New York, 1989.
23. Grigoriu, M. Crossing of non-Gaussian translation process. *J. Engng. Mech., ASCE*, 1984, **110**(4), 610–620.
24. Winterstein, S. R. Nonlinear vibration models for extremes and fatigue. *J. Engng Mech., ASCE*, 1988, **114**(10), 1772–1790.
25. Kac, M. and Siegert, A. J. F. On the theory of noise in radio receivers with square law detectors. *J. Appl. Phys.*, 1947, **8**, 383–397.
26. Naess, A. Statistical analysis of second-order response of marine structures. *J. Ship Res.*, 1985, **29**(4), 270–284.
27. Langley, R. S. A statistical analysis of non-linear random waves. *Ocean Engng*, 1987, **14**, 389–407.
28. Holmes, J. D. Wind Action on glass and Brown's integral. *Engng Struct.*, 1985, **7**, 226–230.
29. Reed, D. A. Influence of non-Gaussian local pressures on cladding glass. *J. Wind Engng and Ind. Aerodyn.*, 1993, **48**, 51–61.
30. Calderone, I. and Melbourne, W. H. The behavior of glass under wind loading. *J. Wind Engng and Ind. Aero.*, 1993, **48**, 81–94.
31. Soize, C. Gust loading factors with nonlinear pressure terms. *J. Structures Div. ASCE*, 1978, **104**(6), 991–1007.
32. Ang, A. H.-S. and Tang, W. H. *Probability Concepts in Engineering Planning & Design, Volume I—Basic Principles*. John Wiley and Sons, Inc., New York, 1975.
33. Cartwright, D. E. and Longuet-Higgins, M. S. The statistical distribution of the maxima of a random function. *Proc. Royal Society of London A*, **237**, 1956, pp. 212-232.
34. Ang, A. H.-S. and Tang, W. H. *Probability Concepts in Engineering Planning & Design, Volume II—Decision, Risk, and Reliability*. John Wiley & Sons, Inc., New York, 1984.
35. Madsen, H. O., Krenk, S. and Lind, N. C. *Methods of Structural Safety*. Prentice Hall, Englewood Cliffs, NJ, 1986.

36. Davenport, A. G. Gust loading factors. *J. Structural Division ASCE*, 1967, **93**(ST3), 11–34.
37. Cheong, H.-F. Estimation of the minimum pressure coefficient due to gusts. *Structural Safety*, **17**, 1995, 1–16.
38. Krayer, W. R. and Marshall, R. D. Gust factors applied to hurricane winds. *Bulletin American Meteorological Society*, 1992, **73**(5), 613–617.
39. Shinozuka, M. Simulation of multivariate and multi-dimensional random processes. *J. Acoust. Soc. Am.*, 1971, **49**, 357–368.
40. Mignolet, M. P. and Spanos, P. D. Recursive simulation of stationary multivariate random processes. *J. Appl. Mech.*, 1987, **54**, 674–687.
41. Li, Y. and Kareem, A. Simulation of multivariate random processes: hybrid DFT and digital filtering approach. *J. Engng Mech., ASCE*, 1993, **119**, 1078–1098.
42. Soong, T. T. and Grigoriu, M. *Random Vibration of Mechanical and Structural Systems*. Prentice Hall, Englewood Cliffs, NJ, 1993.
43. Grigoriu, M. *Applied non-Gaussian Processes*. Prentice Hall, Englewood Cliffs, NJ, 1995.
44. Yamazaki, F. and Shinozuka, M. Digital generation of non-Gaussian stochastic fields. *J. Engng. Mech., ASCE*, 1988, **114**(7), 1183–1197.
45. Gurley, K. and Kareem, A. Simulation of a class of non-normal processes. *Special Volume of the Journal of Nonlinear Mechanics*, EUROMECH-Colloquium No. 329 on Methods for Nonlinear Stochastic Structural Dynamics, 1995.
46. Conner, D. A. and Hammond, J. L. Modeling of stochastic system inputs having prescribed distribution and covariance functions. *Appl. Mathematical Modeling*, 1979, **3**(2), 61–69.
47. Deutsch, R. *Nonlinear Transformations of Random Processes*. Prentice-Hall, Englewood Cliffs, NJ, 1962.
48. Johnson, G. E. Constructions of particular random process. *Proc. IEEE*, 1994, **82**(2), 270–285.
49. Ammon, D. Approximation and generation of Gaussian and non-Gaussian statinary processes. *Structural Safety*, 1990, **8**, 153–160.
50. Kareem, A. Numerical simulation of stochastic wind effects. *Proc. 7th U.S. National Conf. on Wind Engineering*, Vol. 1, Wind Engineering Research Council, LA, 1993.
51. Seong, S. H. and Peterka, J. A. Computer simulation of non-Gaussian wind pressure fluctuations. *Proc. Seventh U.S. National Conf. on Wind Engineering*, **2**, 1993, pp. 623–632.
52. Kobayashi, H., Hatanaka, A. and Ueda, T. Active simulation of time histories of strong wind gust in a wind tunnel. *J. Wind Engng and Ind. Aerol.*, 1994, **53**, 315–330.
53. Read, W. W. and Sobey, R. J. Phase spectrum of surface gravity waves. *J. Waterway, Port, Coastal, and Ocean Engng*, 1987, **48**, 507–522.
54. Borgman, L. E. Irregular ocean waves: kinematics and forces. *The Sea*. Prentice Hall, Englewood Cliffs, NJ, 1990.
55. Vanmarcke, E. H. and Fenton, G. A. Conditional simulation of local fields of earthquake ground motion. *Structural Safety*, 1991, **10**, 247–264.
56. Hoshiya, M. Conditional simulation of a stochastic field. *Proc. 6th Int. Conf. on Structural Safety and Reliability*, Innsbruck, Austria. Balkema Publishers, Amsterdam, Netherlands, 1993.
57. Kameda, H. and Morikawa, H. A conditioned stochastic processes for conditional random fields. *J. Engng Mech., ASCE*, 1994, **120**(4), 855–875.
58. Elishakoff, I., Ren, Y. J. and Shinozuka, M. Conditional simulation of non-Gaussian random fields. *Engng Struct.*, 1994, **16**(7), 558–563.
59. Murlidharan, T. and Kareem, A. Conditional simulation of Gaussian velocity field. Tech. Report no. CEGEOS-93-1, Department of Civil Engineering and Geological Sciences, University of Notre Dame, 1993.
60. Maruyama, T. and Marikawa, H. Digital simulation of wind fluctuations in boundary layer using experimental data. Wind Engineering, Retrospect and Prospect, *Proc. Ninth Int. Conf. on Wind Engineering*, New Delhi, India, January 9–13, **2**, 1995.
61. Newland, D. E. *An introduction to Random Vibrations, Spectral & Wavelet Analysis*. Longman Scientific & Technical, and John Wiley & Sons, New York, 1993.
62. Kareem, A., Gurley, K. and Kantor, J. C. Time-scale analysis of nonstationary processes utilizing wavelet transforms. *Proc. 67th Int. Conf. on Structural Safety and Reliability*, Innsbruck, Austria. Balkema Publishers, Amsterdam, Netherlands, 1993.
63. Kameda, H. Evolutionary spectra of siesmogram by multifilter. *J. Engng Mech. Div., ASCE*, 1975, **101**(EM6), 787–801.
64. Rioul, O. and Duhamel, P. Fast algorithms for discrete and continuous wavelet transforms. *IEEE Trans. Information Theory*, 1992, **38**, 569–586.
65. Saragoni, G. R. and Hart, G. C. Simulation of artificial earthquakes. *Earthquake Engng Struct. Dyn.*, 1974, **2**, 249–267.
66. Li, Y. and Kareem, A. Simulation of multivariate non-stationary random processes by FFT. *J. Engng Mech., ASCE*, 1991, **117**, 1037–1058.
67. Gurley, K. and Kareem, A. On the analysis and simulation of random processes utilizing higher order spectra and wavelet transforms. *Proc. Second Int. Conf. on Computational Stochastic Mechanics*, Athens, Greece. Balkema Publishers, Amsterdam, Netherhalds, 1994.